Inorg. Chem. **2008**, *47*, 6804−6824

Molecular and Electronic Structures of Mononuclear Iron Complexes Using Strongly Electron-Donating Ligands and their Oxidized Forms

Julia B. H. Strautmann,[†] Serena DeBeer George,[‡] Eberhard Bothe,[§] Eckhard Bill,[§] Thomas Weyhermüller,[§] Anja Stammler,[†] Hartmut Bögge,[†] and Thorsten Glaser*[,†]

Fakultät für Chemie, Universität Bielefeld, Universitätsstrasse 25, D-33615 Bielefeld, Germany, Stanford Synchrotron Radiation Laboratory, SLAC, Stanford University, Stanford, California 94309, and Max-Planck-Institut für Bioanorganische Chemie, Stiftstrasse 34-36, D-45470 Mülheim, Germany

Received February 28, 2008

The ligand L^{2-} (H_2L = *N,N′*-dimethyl-*N,N′*-bis(3,5-di-*t*-butyl-2-hydroxybenzyl)-1,2-diaminoethane) has been employed for the synthesis of two mononuclear Fe^{III} complexes, namely, [LFe(η^2-NO_3)] and [LFeCl]. L^{2-} is comprised of four strongly electron-donating groups (two *tert*-amines and two phenolates) that increase the electron density at the coordinated ferric ions. This property should facilitate oxidation of the complexes, that is, stabilization of the oxidized species. The molecular structures in the solid state have been established by X-ray diffraction studies. [LFeCl] is five-coordinate in a square-pyramidal coordination environment with the ligand adopting a *trans*-conformation, while [LFe(η^2-NO_3)] is six-coordinate in a distorted octahedral environment with the ligand in a β-cis conformation. The electronic structures have been studied using magnetization, EPR, Mössbauer (with and without applied field), UV−vis−NIR, and X-ray absorption spectroscopies, which demonstrate highly anisotropic covalency from the strong σ- and π-donating phenolates. This analysis is supported by DFT calculations on [LFeCl]. The variations of the well-understood spectroscopic data in the solid state to the spectroscopic data in solution have been used to obtain insight in the molecular structure of the two complexes in solution. While the molecular structures of the solid states are retained in solutions of nonpolar aprotic solvents, there is, however, one common molecular structure in all protic polar solvents. The analysis of the LMCT transitions and the rhombicity *E*/*D* clearly establish that both compounds exhibit a β-cis conformation in these protic polar solvents. These two open coordination sites, cis to each other, allow access for two potential ligands in close proximity. Electrochemical analysis establishes two reversible oxidation waves for [LFeCl] at +0.55 V and +0.93 V vs Fc^+/Fc and one reversible oxidation wave at +0.59 V with an irreversible oxidation at +1.07 V vs Fc^+/Fc for [LFe(η^2-NO_3)]. The one- and the two-electron oxidations of [LFeCl] by chronoamperometry have been followed spectroscopically. The increase of a strong band centered at 420 nm indicates the formulation of $[LFeCl]^+$ as a Fe^{III} monophenoxyl radical complex and of $[LFeCl]^{2+}$ as a Fe^{III} bisphenoxyl radical complex. These studies imply that the ligand L^{2-} is capable of providing a flexible coordination geometry with two binding sites for substrates and the allocation of two oxidation equivalents on the ligand.

1. Introduction

The catalytic cycles of dioxygen-activating metalloenzymes often employ high-valent intermediates that store two oxidation equivalents.[1–3] In polynuclear active sites, these may be stored primarily on the metal centers (e.g., methane monooxygenase[1,4–6] /$Fe^{IV}Fe^{IV}$), whereas they are usually evenly distributed on the ligand and on the metal in

* To whom correspondence should be addressed. E-mail: thorsten.glaser@uni-bielefeld.de (T.G.).
[†] Universität Bielefeld.
[‡] Stanford University.
[§] Max-Planck-Institut für Bioanorganische Chemie.

(1) Solomon, E. I.; Brunold, T. C.; Davis, M. I.; Kemsley, J. N.; Lee, S.-K.; Lehnert, N.; Neese, F.; Skulan, A. J.; Yang, Y.-S.; Zhou, J. *Chem. Rev.* **2000**, *100*, 235–349.
(2) Costas, M.; Mehn, M. P.; Jensen, M. P.; Que, L., Jr. *Chem. Rev.* **2004**, *104*, 939–986.
(3) Sono, M.; Roach, M. P.; Coulter, E. D.; Dawson, J. H. *Chem. Rev.* **1996**, *96*, 2841–2887.
(4) Shu, L.; Nesheim, J. C.; Kauffmann, K.; Münck, E.; Lipscomb, J. D.; Que, L., Jr. *Science* **1997**, *275*, 515–518.
(5) Wallar, B. J.; Lipscomb, J. D. *Chem. Rev.* **1996**, *96*, 2625–2657.
(6) Rosenzweig, A. C.; Frederick, C. A.; Lippard, S. J.; Nordlund, P. *Nature* **1993**, *366*, 537–543.

10.1021/ic800335t CCC: $40.75
Published on Web 06/27/2008

mononuclear active sites (e.g., galactose oxidase[7–9] /Cu^{II} phenoxyl radical or mononuclear iron heme sites like cytochrome P450 compound I[10–19] /Fe^{IV}═O porphyrin cation radical). A pure metal-centered storage of two oxidation equivalents on one metal center has also recently been shown for taurine α-ketoglutarate-dependent dioxygenase (TauD), which involves oxidation of Fe^{II} and formation of a high valent Fe^{IV}═O intermediate.[20–23]

There have been many successful attempts to model nonheme mononuclear Fe^{IV}═O species.[24–29] Recently, a macrocyclic ligand incorporating four *tert*-amines and one thiolate as donor groups has been employed,[30] as well as a diazaadamantane-derived ligand[31] and tetraamido macrocyclic ligands.[32,33] All of these complexes are composed of mainly redox-innocent ligands that facilitate metal-centered oxidation.

In the last two decades, it has been increasingly realized by inorganic chemists[34–37] that oxidations of transition metal complexes can also be ligand-centered. Such ligands have been termed "noninnocent ligands". In particular, for metal phenolate complexes, Wieghardt et al. have shown that the oxidation process can be metal- or ligand-centered, depending on the specific metal and the phenolate substitution pattern. However, regardless of the localization of the oxidation, oxidized metal-phenolate sites might be used for interesting oxidative transformations as catalyzed by galactose oxidase[7–9,38,39] and cytochrome P450.[10–12,25] Recently, there have also been investigations of the oxidation characteristics of mononuclear complexes using tetradentate ligands composed of two nitrogen and two noninnocent phenolate donors. Pratt and Stack have investigated the differences in the electronic structure and in the redox and catalytic properties of salen-derived (H_2salen = *N*,*N*′-bis(salicylidene)-ethylendiamine, incorporating two imine-nitrogen donors) and salan-derived (H_2salan = *N*,*N*′-bis(*o*-hydroxybenzyl)-ethylendiamine, incorporating two amine-nitrogen donors) Cu^{II} complexes (Scheme 1).[39,40] These studies revealed that the complex [(salan′)Cu] is easier to oxidize (+80 mV vs Fc^+/Fc) than the corresponding [(salen′)Cu] complex (+450 mV vs Fc^+/Fc). They have proposed that the oxidation is not metal-centered (yielding a Cu^{III} species) but ligand-centered (yielding a Cu^{II} phenoxyl radical species). Similar studies without generating the oxidized species have been performed with mononuclear Cu^{II} complexes of the ligand L^{2-} and closely related ligands.[41]

Fujii et al. have used Fe^{III} salen* (Scheme 1) complexes and investigated their electronic structure and electrochemical behavior.[42] They also proposed that the oxidation yields Fe^{III} phenoxyl radical species.

Our strategy for stabilization of highly oxidized diiron complexes involves the use of strongly electron-donating ligands.[43] This will lead to highly covalent Fe−ligand bonds and increased electron density at the iron atoms facilitating the generation of highly oxidized complexes. The ligand design is mainly based on the results of Que et al. They succeeded in fully characterizing a high-valent Fe^{III}–(μ_2-O)$_2$–Fe^{IV} complex using a substituted tpa ligand (tpa = tris(2-

(7) Ito, N.; Phillips, S. E. V.; Yadav, K. D. S.; Knowles, P. F. *J. Mol. Biol.* **1994**, *238*, 794–814.
(8) Whittaker, J. W.; Whittaker, M. M. *Pure Appl. Chem.* **1998**, *70*, 903–910.
(9) Whittaker, J. W. *Chem. Rev.* **2003**, *103*, 2347–2363.
(10) Davydov, R.; Makris, T. M.; Kofman, V.; Werst, D. E.; Sligar, S. G.; Hoffman, B. M. *J. Am. Chem. Soc.* **2001**, *123*, 1403–1415.
(11) Kellner, D. G.; Hung, S.-C.; Weiss, K. E.; Sligar, S. G. *J. Biol. Chem.* **2002**, *277*, 9641–9644.
(12) Denisov, I. G.; Makris, T. M.; Sligar, S. G.; Schlichting, I. *Chem. Rev.* **2005**, *105*, 2253–2277.
(13) Theorell, H.; Ehrenberg, A. *Arch. Biochem. Biophys.* **1952**, *41*, 442–461.
(14) Moss, T.; Ehrenberg, A.; Bearden, A. J. *Biochemistry* **1969**, *8*, 4159–4162.
(15) Schulz, C. E.; Rutter, R.; Sage, J. T.; Debrunner, P. G.; Hager, L. P. *Biochemistry* **1984**, *23*, 4743–4754.
(16) Rutter, R.; Hager, L. P.; Dhonau, H.; Hendrich, M.; Valentine, M.; Debrunner, P. G. *Biochemistry* **1984**, *23*, 6809–6816.
(17) Nam, W. *Acc. Chem. Res.* **2007**, *40*, 522–531.
(18) Groves, J. T.; Haushalter, R. C.; Nakamura, M.; Nemo, T. E.; Evans, B. J. *J. Am. Chem. Soc.* **1981**, *103*, 2884–2886.
(19) Mandon, D.; Weiss, R.; Jayaraj, K.; Gold, A.; Terner, J.; Bill, E.; Trautwein, A. X. *Inorg. Chem.* **1992**, *31*, 4404–4409.
(20) Price, J. C.; Barr, E. W.; Tirupati, B.; Bollinger, J. M., Jr.; Krebs, C. *Biochemistry* **2003**, *42*, 7497–7508.
(21) Riggs-Gelasco, P. J.; Price, J. C.; Guyer, R. B.; Brehm, J. H.; Barr, E. W.; Bollinger, J. M., Jr.; Krebs, C. *J. Am. Chem. Soc.* **2004**, *126*, 8108–8109.
(22) Proshlyakov, D. A.; Henshaw, T. F.; Monterosso, G. R.; Ryle, M. J.; Hausinger, R. P. *J. Am. Chem. Soc.* **2004**, *126*, 1022–1023.
(23) Bollinger, J. M., Jr.; Price, J. C.; Hoffart, L. M.; Barr, E. W.; Krebs, C. *Eur. J. Inorg. Chem.* **2005**, 4245–4254.
(24) Grapperhaus, C. A.; Mienert, B.; Bill, E.; Weyhermüller, T.; Wieghardt, K. *Inorg. Chem.* **2000**, *39*, 5306–5317.
(25) Rohde, J.-U.; In, J.-H.; Lim, M. H.; Brennessel, W. W.; Bukowski, M. R.; Stubna, A.; Münck, E.; Nam, W.; Que, L., Jr. *Science* **2003**, *299*, 1037–1039.
(26) Martinho, M.; Banse, F.; Bartoli, J.-F.; Mattioli, T. A.; Battioni, P.; Horner, O.; Bourcier, S.; Girerd, J.-J. *Inorg. Chem.* **2005**, *44*, 9592–9596.
(27) Kaizer, J.; Klinker, E. J.; Oh, N. Y.; Rohde, J.-U.; Song, W.; Stubna, A.; Kim, J.; Münck, E.; Nam, W.; Que, L., Jr. *J. Am. Chem. Soc.* **2004**, *126*, 472–473.
(28) Privett, H. K.; Reedy, C. J.; Kennedy, M. L.; Gibney, B. R. *J. Am. Chem. Soc.* **2002**, *124*, 6828–6829.
(29) Special issue on dioxygen activation by metalloenzymes and models *Acc. Chem. Res.* **2007**, *40*, 465–634.
(30) Bukowski, M. R.; Koehntop, K. D.; Stubna, A.; Bominaar, E. L.; Halfen, J. A.; Münck, E.; Nam, W.; Que, L., Jr. *Science* **2005**, *310*, 1000–1002.
(31) Bautz, J.; Bukowski, M. R.; Kerscher, M.; Stubna, A.; Comba, P.; Lienke, A.; Münck, E.; Que, L., Jr. *Angew. Chem., Int. Ed.* **2006**, *45*, 5681–5684.
(32) Ghosh, A.; de Oliveira, F. T.; Yano, T.; Nishioka, T.; Beach, E. S.; Kinoshita, I.; Münck, E.; Ryabov, A. D.; Horwitz, C. P.; Collins, T. J. *J. Am. Chem. Soc.* **2005**, *127*, 2505–2513.
(33) Chanda, A.; Popescu, D.-L.; de Oliveira, F. T.; Bominaar, E.; Ryabov, A. D.; Münck, E.; Collins, T. J. *J. Inorg. Biochem.* **2006**, *100*, 606–619.
(34) Adam, B.; Bill, E.; Bothe, E.; Goerdt, B.; Haselhorst, G.; Hildenbrand, K.; Sokolowski, A.; Steenken, S.; Weyhermüller, T.; Wieghardt, K. *Chem.—Eur. J.* **1997**, *3*, 308–319.
(35) Sokolowski, A.; Bothe, E.; Bill, E.; Weyhermüller, T.; Wieghardt, K. *Chem. Comm.* **1996**, 1671–1672.
(36) Müller, J.; Weyhermüller, T.; Bill, E.; Hildebrandt, P.; Ouldmoussa, L.; Glaser, T.; Wieghardt, K. *Angew. Chem., Int. Ed.* **1998**, *37*, 616–619.
(37) Chaudhuri, P.; Wieghardt, K. *Prog. Inorg. Chem.* **2001**, *50*, 151–216.
(38) Chaudhuri, P.; Hess, M.; Müller, J.; Hildenbrand, K.; Bill, E.; Weyhermüller, T.; Wieghardt, K. *J. Am. Chem. Soc.* **1999**, *121*, 9599–9610.
(39) Pratt, R. C.; Stack, T. D. P. *J. Am. Chem. Soc.* **2003**, *125*, 8716–8717.
(40) Pratt, R. C.; Stack, T. D. P. *Inorg. Chem.* **2005**, *44*, 2367–2375.
(41) Vaidyanathan, M.; Palaniandavar, M.; Gopalan, R. S. *Indian J. Chem.* **2003**, *42A*, 2210–2222.
(42) Kurahashi, T.; Kobayashi, Y.; Nagamoto, S.; Tosha, T.; Kitagawa, T.; Fujii, H. *Inorg. Chem.* **2005**, *44*, 8156–8166.
(43) De Oliveira, F. T.; Chanda, A.; Banerjee, D.; Shan, X.; Mondal, S.; Que, L., Jr.; Bominaar, E. L.; Münck, E.; Collins, T. J. *Science* **2007**, *315*, 835–838.

Scheme 1

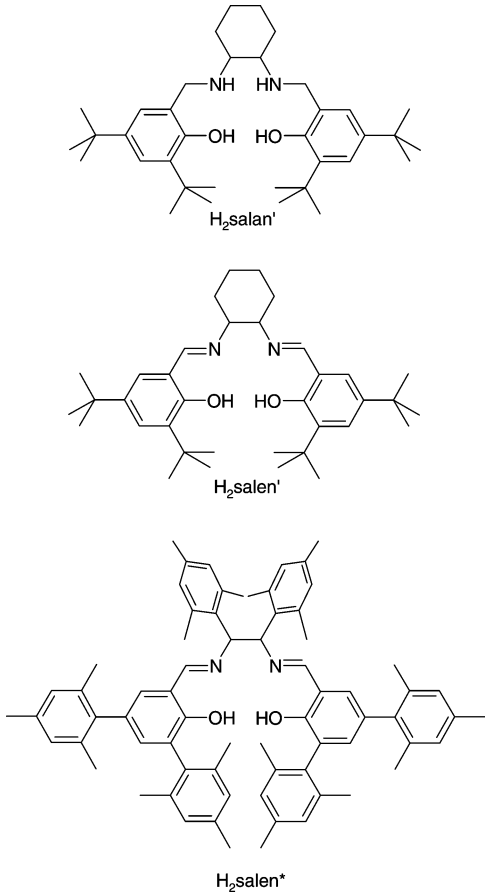

Scheme 2

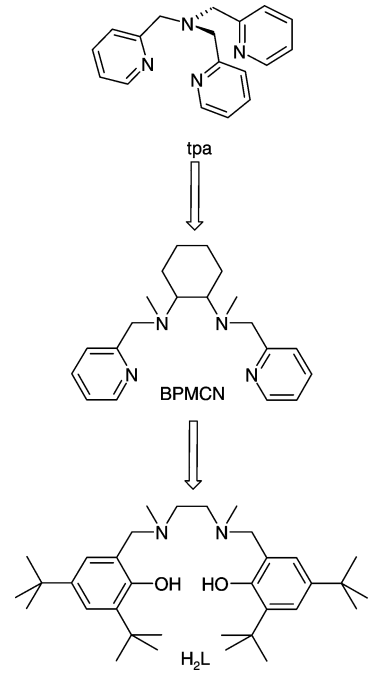

pyridylmethyl)amine) (Scheme 2).[44,45] Later, they used linear tetradentate ligands like BPMCN (Scheme 2),[46,47] which correspond to a change of the ligand topology and a substitution of a pyridine donor by a *tert*-amine donor. Pyridine is a relatively weak σ-donor ligand that also has some π-acceptor capabilities, thus reducing the electron-density at the metal atom to which it is coordinated. However, recently they have succeeded in the electrochemical generation and characterization of a tpa-based $Fe^{IV}-(\mu_2\text{-}O)_2-Fe^{IV}$ complex.[48]

Our approach is based on the formal substitution of the remaining weak pyridine donors by strong σ- and π-donors like phenolates to further stabilize such highly oxidized species. To prevent radical initiated decomposition, the *o*- and *p*-positions of the phenolates incorporated in the ligand should be blocked; hence the ligand H_2L we use contains *t*-butyl groups in *o*- and *p*-positions (Scheme 2). Because the *t*-butyl groups are electron-donating, this will also increase the electron-donating capabilities of the phenolates. Moreover, we use *tert*-amines which have been shown to further stabilize high-valent Fe^{IV}=O complexes.[46] However, the origin of this stabilization is still controversial.[49,50]

Accordingly, we have used ligand H_2L[51,52] to synthesize the dinuclear ferric complex [LFe(μ_2-O)FeL].[53,54] [LFe(μ_2-O)FeL] exhibits two reversible oxidation waves at +0.27 V and +0.44 V vs Fc^+/Fc. To the best of our knowledge, these are the lowest redox potentials reported for the oxidation of an oxo-bridged dinuclear ferric complex. Thus, a species $[LFe(\mu_2\text{-}O)FeL]^{2+}$, accumulating the same number of oxidizing equivalents as the intermediate **Q** of MMO seems to be accessible. This supports our working hypothesis that the ligand L^{2-} is strongly electron-donating and therefore capable of stabilizing highly oxidized diiron units. We have generated the single oxidized $[LFe(\mu_2\text{-}O)FeL]^+$ and the doubly oxidized $[LFe(\mu_2\text{-}O)FeL]^{2+}$ electrochemically and chemically and studied their electronic structures as well as their follow-up reactivity.[54] However, it became evident that mononuclear species form.

Therefore, we have synthesized the mononuclear complexes [LFe(η^2-NO_3)] and [LFeCl] as reference compounds. The $N_2(O^{Ph})_2X$ coordination environments closely resemble

(44) Dong, Y.; Fujii, H.; Hendrich, M. P.; Leising, R. A.; Pan, G.; Randall, C. R.; Wilkinson, E. C.; Zang, Y.; Que, L., Jr.; Fox, B. G.; Kauffmann, K.; Münck, E. *J. Am. Chem. Soc.* **1995**, *117*, 2778–2792.
(45) Hsu, H.-F.; Dong, Y.; Shu, L.; Young, V. G. J.; Que, L., Jr. *J. Am. Chem. Soc.* **1999**, *121*, 5230–5237.
(46) Costas, M.; Rohde, J.-U.; Stubna, A.; Ho, R. Y. N.; Quaroni, H.; Münck, E.; Que, L., Jr. *J. Am. Chem. Soc.* **2001**, *123*, 12931–12932.
(47) Jensen, M P.; Costas, M.; Ho, R. Y. N.; Kaizer, J.; Mairata i Payeras, A.; Münck, E.; Que, L., Jr.; Rohde, J.-U.; Stubna, A. *J. Am. Chem. Soc.* **2005**, *127*, 10512–10525.
(48) Xue, G.; Wang, D.; De Hont, R.; Fiedler, A. T.; Shan, X.; Münck, E.; Que, L., Jr. *Proc. Natl. Acad. Sci.* **2007**, *104*, 20713–20718.
(49) Meyerstein, D. *Coord. Chem. Rev.* **1999**, *185−186*, 141–147.
(50) Berry, J. F.; Bill, E.; García-Serres, R.; Neese, F.; Weyhermüller, T.; Wieghardt, K. *Inorg. Chem.* **2006**, *45*, 2027–2037.
(51) Tshuva, E. Y.; Goldberg, I.; Kol, M. *J. Am. Chem. Soc.* **2000**, *122*, 10706–10707.
(52) Balsells, J.; Carroll, P. J.; Walsh, T. J. *Inorg. Chem.* **2001**, *40*, 5568–5574.
(53) Glaser, T.; Pawelke, R. H.; Heidemeier, M. *Z. Anorg. Allg. Chem.* **2003**, *629*, 2274–2281.
(54) Strautmann, J. B. H.; Frhr. von Richthofen, C.-G.; DeBeer George, S.; Bothe, E.; Bill, E.; Glaser, T. Unpublished work.
(55) Ohlendorf, D. H.; Orville, A. M.; Lipscomb, J. D. *J. Mol. Biol.* **1994**, *244*, 586–608.
(56) Ohlendorf, D. H.; Lipscomb, J. D.; Weber, P. C. *Nature* **1988**, *336*, 403–405.

that of protocatechuate 3,4-dioxygenase (3,4-PCD), which is a mononuclear nonheme intradiol-cleaving catechol dioxygenase.[1,2,55,56] Herein, we use X-ray crystallography, magnetic susceptibility, DFT calculations, electronic absorption-, EPR-, X-ray absorption-, and Mössbauer (with and without an applied field) spectroscopies to describe their molecular and electronic structure in the solid state, as well as in solution in detail. In addition, we report on the electro- and spectro-electrochemistry of [LFe(η^2-NO_3)] and [LFeCl] and the reversible oxidation of [LFeCl] to the Fe^{III} bisphenoxyl radical $[LFeCl]^{2+}$.

2. Experimental Section

2.1. Preparations of Compounds. H_2L was synthesized as described previously.[53]

[LFe(η^2-NO_3)]. A solution of $Fe(NO_3)_3 \cdot 9H_2O$ (772 mg, 1.92 mmol) in ethanol (50 mL) was added dropwise to a solution of H_2L (1.00 g, 1.92 mmol) in acetone (50 mL). The dark blue solution was stirred for ten minutes, and a solution of triethylamine (0.54 mL, 3.7 mmol) in ethanol (30 mL) was added dropwise. The blue solution was heated to reflux for two hours. After cooling, water (100 mL) was added dropwise. The blue precipitate was filtered off and dried under high vacuum. Diffusion of petroleum ether into a solution of the product in *t*-butylmethylether gave dark blue needles suitable for X-ray crystal structure analysis. Yield: 676 mg (60%). MS-MALDI-TOF: m/z = 640 (40) $[M]^+$, 578 (100) $[M - NO_3]^+$. IR(KBr): $\tilde{\nu}/cm^{-1}$ = 2956s, 2904m, 2868m, 1634w, 1520s, 1467s, 1441s, 1413m, 1385s, 1361m, 1305m, 1265s, 1248s, 1203m, 1169m, 875w, 836m, 810w, 750m, 611w, 559m, 486w. IR (DCM): $\tilde{\nu}/cm^{-1}$ = 2964m, 2905m, 2868w, 1712w, 1605w, 1524s, 1466s, 1442s, 1413m, 1356s, 1304m, 1204w, 1170w, 879w, 843m, 810w, 763s, 612w, 558m, 485w. Anal. Calcd for [LFe(η^2-NO_3)]·$0.4C_5H_{12}$: C 64.58, H 8.85, N 6.28. Found: C 64.37, H 9.01, N 6.13.

[LFeCl]. A solution of $FeCl_3$ (247 mg, 1.52 mmol) in acetonitrile (15 mL) and a solution of tetramethylammoniumhydroxide (2.2 M in methanol, 122 mg, 3.04 mmol) in acetonitrile (5 mL) were added to a suspension of H_2L (800 mg, 1.52 mmol) in acetonitrile (35 mL). The purple solution was heated to reflux for two hours and filtered after cooling. By slow evaporation of the solvent, purple crystals of [LFeCl] suitable for X-ray crystal structure analysis and colorless crystals of H_2L formed within a few weeks. They were filtered off and dissolved in chloroform/*n*-heptane (1:1, 100 mL). The solution was filtered, and the solvent was evaporated slowly. Within a few weeks, crystals of [LFeCl] suitable for X-ray crystal structure analysis contaminated with some crystalline H_2L at the surface formed. Yield: 421 mg (45%). MS-MALDI-TOF: m/z = 613 (77) $[M]^+$, 578 (100) $[M - Cl]^+$, 524 (7) $[H_2L]^+$. IR (KBr): $\tilde{\nu}/cm^{-1}$ = 2954s, 2904s, 2868m, 1603w, 1466s, 1442s, 1413m, 1391w, 1361m, 1307m, 1268s, 1244s, 1204m, 1169m, 1129w, 1068w, 1056w, 999w, 928w, 914w, 876m, 840m, 811w, 766w, 749m, 607w, 552m, 486w. Anal. Calcd for [LFeCl]·$0.09H_2L$·$0.07CHCl_3$: C 66.59, H 8.90, N 4.60. Found: C 66.77, H 8.67, N 4.41.

2.2. X-Ray Crystallographic Data Collection and Refinement of the Structures. Dark blue/purple single-crystals of [LFe(η^2-NO_3)]·$0.5C_5H_{12}$, [LFeCl]·$CHCl_3$, and [LFeCl]·$2CH_3CN$ were coated with perfluoropolyether, picked up with nylon loops (thin glass fiber for [LFeCl]·$CHCl_3$), and immediately mounted in the nitrogen cold stream of the diffractometers to prevent loss of solvent. Diffractometers were equipped with a Mo-target rotating-anode X-ray source (sealed Mo tube for [LFeCl]·$CHCl_3$) and a graphite monochromator (Mo Kα, λ = 0.71073 Å). Final cell constants were obtained from least-squares fits of all (8192 for [LFeCl]·$CHCl_3$) measured reflections. Intensity data were corrected for absorption using intensities of redundant reflections (SADABS 2.03). The structures were readily solved by direct methods and subsequent difference Fourier techniques (SHELXS/L, SADABS, G.M. Sheldrick, University of Göttingen 1997/2001). All non-hydrogen atoms (except the disordered solvent atoms for [LFeCl]•$CHCl_3$) were refined anisotropically. Hydrogen atoms were placed at calculated positions and refined as riding atoms with isotropic displacement parameters.

A pentane solvent molecule in crystals of [LFe(η^2-NO_3)]·$0.5C_5H_{12}$ was found to be severely disordered. The molecule was split on three positions with an occupation ratio of 40:30:30. Corresponding carbon atoms of the split model were refined with equal anisotropic displacement parameters (EADP) and C−C bond distances were restrained to be equal within errors using the SADI and DFIX instructions of SHELXL. A disordered *t*-butyl group (C27−C30) in one of the two crystallographically independent complex molecules was split on two positions with restrained bond distances (SADI) and occupation factors of 0.69 and 0.31. Relatively high residual density peaks (≤2 e $Å^{-3}$) indicated a second, probably not fully occupied solvent position next to a center of inversion which could not be refined due to extreme disorder.

The chloroform molecule in crystals of [LFeCl]·$CHCl_3$ was also found to be disordered. One carbon and three chlorine positions could be refined with half-occupancy and restrained C−Cl and Cl−Cl distances, representing one-half $CHCl_3$ molecule. Close to this five additional positions could be refined as chlorine, each with an occupancy of 0.3. The corresponding carbon position could not be localized.

Disorder was also detected in the structure of [LFeCl]·$2CH_3CN$, where a *t*-butyl group (C27−C30) was found to be disordered over two sites. The positions were split in a 59:41 ratio with equal displacement parameters and restrained bond lengths (EADP, SADI). One of the two acetonitrile molecules was disordered and split on two positions which were refined with restrained bond distances and thermal parameters (DFIX, EADP).

Crystal data and further details concerning the crystal structure determination are found in Table 1.

2.3. Other Physical Measurements. Infrared spectra (400−4000 cm^{-1}) of solid samples were recorded either on a Bruker Vector 22 spectrometer or on a Shimadzu FTIR 8300 as KBr disks or in CH_2Cl_2 solutions. UV−vis–NIR absorption spectra of solutions were measured on a Varian Cary 50 spectrophotometer in the range 190−1100 nm at ambient temperatures. MALDI-TOF mass spectra using DCTB (DCTB = 2-((2*E*)-3-(4-*t*-butylphenyl)-2-methylprop-2-enylidene)malono-nitrile) as the matrix were recorded on a Bruker Reflex IV mass spectrometer. Cyclic and square-wave voltammograms were measured by use of an EG&G potentiostat/galvanostat 273A on Ar-flushed CH_2Cl_2 solutions containing 0.2 M $[NBu_4]PF_6$ as supporting electrolyte in a conventional electrochemical cell. The working electrode was a glassy carbon disk electrode; the counter electrode was a platinum wire, and the reference electrode was Ag/0.01 M $AgNO_3/CH_3CN$. The potentials are referenced versus the ferrocenium/ferrocene (Fc^+/Fc) couple used as an internal standard. Spectroelectrochemical measurements were performed by using an optically transparent thin-layer electrochemical cell (OTTLE cell, d = 0.018 cm). During oxidations/reductions in the OTTLE cell spectral changes were recorded on a Hewlett-Packard HP 8453 diode array spectrophotometer in the range of 190−1100 nm.

Magnetic susceptibility data were measured from powder samples of solid material in the temperature range of 2−300 K with a SQUID susceptometer (MPMS-7, Quantum Design) with a field of 1.0 T. Multiple-field variable-temperature magnetization mea-

Table 1. Crystallographic Data for [LFe(η^2-NO_3)]·0.5C_5H_{12}, [LFeCl]·$CHCl_3$, and [LFeCl]·2CH_3CN

	[LFe(η^2-NO_3)]·0.5C_5H_{12}	[LFeCl]·$CHCl_3$	[LFeCl]·2CH_3CN
chemical formula	$C_{36.5}H_{60}FeN_3O_5$	$C_{35}H_{55}Cl_4FeN_2O_2$	$C_{38}H_{60}ClFeN_4O_2$
fw	676.73	733.46	696.20
T (K)	100(2)	183(2)	100(2)
space group	$P\bar{1}$	$C2/c$	$C2/c$
a (Å)	11.5748(3)	33.2785(10)	32.385(2)
b (Å)	12.5090(4)	14.0224(4)	14.0543(5)
c (Å)	28.7323(9)	18.1858(5)	17.8846(8)
α (deg)	98.638(5)	90	90
β (deg)	92.331(5)	101.7260(10)	99.490(5)
γ (deg)	104.405(5)	90	90
V (Å^3)	3970.4(2)	8309.2(4)	8028.7(7)
Z	4	8	8
ρ_{calcd} (g cm^{-3})	1.132	1.173	1.152
λ (Å)/μ(Mo Kα) (mm^{-1})	0.71073/0.420	0.71073/0.649	0.71073/0.477
crystal size (mm)	0.30 × 0.13 × 0.10	0.40 × 0.28 × 0.10	0.27 × 0.14 × 0.08
reflns collected/2Θ_{max}	65 764/61.98	33 858/54.02	12 0454/60.00
unique reflns	24 806 (R_{int} = 0.0353)	8995 (R_{int} = 0.0214)	11 696 (R_{int} = 0.0733)
obsd reflns ($I > 2\sigma(I)$)	20 887	7317	9866
max./min. transm	0.953/0.861	0.938/0.781	0.956/0.848
data/restraints/params	24 806/78/860	8995/6/436	11 696/36/448
GOF[a]	1.085	1.077	1.145
R1[b], wR2[c] ($I > 2\sigma(I)$)	0.0583, 0.1617	0.0610, 0.1789	0.0624, 0.1453
residual density (e Å^{-3})	+1.901 and −0.991	0.878 and −0.748	+0.686 and −0.550

[a] GOF = $[\sum[w(F_o^2 - F_c^2)^2]/(n-p)]^{1/2}$. [b] R1 = $\sum||F_o| - |F_c||/\sum|F_o|$. [c] wR2 = $[\sum[w(F_o^2 - F_c^2)^2]/\sum[w(F_o^2)^2]]^{1/2}$, where $w = 1/\sigma^2(F_o^2) + (aP)^2 + bP$, $P = (F_o^2 + 2F_c^2)/3$.

surements were done at 1 T, 4 T, and 7 T, also in the range of 2−300 K with the magnetization equidistantly sampled on a 1/T temperature scale. The experimental data were corrected for underlying diamagnetism by use of tabulated Pascal's constants, as well as for temperature-independent paramagnetism. The susceptibility and magnetization data of the ferric high-spin complexes ($S = 5/2$) were analyzed on the basis of the usual spin-Hamiltonian description for the electronic ground-state by using our own simulation package julX written by E.B. for exchange coupled systems.[57] The Hamilton operator was

$$\hat{H} = g\beta\hat{\vec{S}}\cdot\vec{B} + D[\hat{S}_z^2 - 1/3S(S+1) + E/D(\hat{S}_x^2 - \hat{S}_y^2)] \quad (1)$$

where g is the average electronic g value, D the axial zero-field splitting parameter, and E/D is the rhombicity parameter. Magnetic moments were obtained from numerically generated derivatives of the eigenvalues of eq 1, and summed up over 16 field orientations along a 16-point Lebedev grid to account for the powder distribution of the sample. Intermolecular interactions were considered by using a Weiss temperature, θ_W, as perturbation of the temperature scale, $kT' = k(T - \theta_W)$.

EPR spectra of frozen solutions and powdered solids were recorded on a Bruker ELEXSYS E500 X-band cw-spectrometer equipped with a helium flow cryostat (Oxford Instruments ESR 910). The resonator was a standard rectangular cavity ER4102. The spectra were simulated by using eq 1 with our program ESIM written by E.B. for powder spectra,[58] which was developed from the routines of Gaffney and Silverstone[59] and which specifically makes use of the Newton−Raphson iterative method described there for the calculation of transition fields. Distributions of E/D (or alternatively D) were taken into account by summation of a series of powder spectra for which the distribution parameter was equidistantly sampled in the range of ±3 of a Gaussian distribution. Usually twenty spectra were superimposed in this procedure. In one case, hyperfine splitting was observed for the EPR line at one distinct effective g value. This was included in a first-order perturbation approximation. Distinct features in the experimental EPR spectra of [LFeCl] led us to try out the effect of a phenomenological fourth-order term in the spin Hamiltonian which was otherwise neglected

$$\hat{O}_4 = 2/3B_4[\hat{O}_4^0 + 20\sqrt{2}\hat{O}_4^3] + B_4^0\hat{O}_4^0 \quad (2)$$

The $\hat{O}_4$ symbols represent equivalent operators of fourth degree in S, and the parameters B_4 and B_4^0 parametrize cubic and trigonal contributions to the ZFS.[60]

Mössbauer data were recorded on a spectrometer with alternating constant acceleration. The minimum experimental line width was 0.24 mm/s (full width at half-height). The sample temperature was maintained constant either in an Oxford Instruments Variox or an Oxford Instruments Mössbauer-Spectromag cryostat. The latter is a split-pair superconducting magnet system for applied fields up to 8 T where the temperature of the sample can be varied in the range from 1.5 to 250 K. The field at the sample is perpendicular to the γ-beam. The ^{57}Co/Rh source (1.8 GBq) was positioned at room temperature inside the gap of the magnet system at a position with field zero. Isomer shifts are quoted relative to iron metal at 300 K. The magnetic Mössbauer spectra were simulated by using the program MX written by E.B.,[61] which is also based on the electronic spin Hamiltonian given in eq 1, and the usual nuclear Hamiltonian for ^{57}Fe with ground-state spin $I = 1/2$ and excited state $I = 3/2$.[62] The simulation routines julX, ESIM, and MX for magnetic susceptibility, EPR, and magnetic Mössbauer simulations, respectively, are accomplished with a SIMPLEX fitting shell for automatic parameter optimization.[63]

XAS data were recorded at the Stanford Synchrotron Radiation Laboratory (SSRL) on focused beam line 9−3, under ring conditions of 3 GeV and 60–100 mA. A Si(220) double-crystal

(57) The program package julX was used for spin-Hamiltonian simulations and fitting the susceptibility data by a full-matrix diagonalization approach; Bill, E. unpublished results.

(58) The program package ESIM was used for simulation of the EPR spectra by a full-matrix diagonalization approach of the appropriate spin-Hamiltonian. Bill, E. Unpublished work.

(59) Gaffney, B. J.; Silverstone, H. J. In *Biological Magnetic Resonance*; Berliner, L. J. , Reuben, J., Eds.; Plenum Press: New York, 1993; Vol. 13.

(60) Abragam, A.; Bleaney, B. *Electron Paramagnetic Resonance of Transition Ions*; Oxford University Press: Oxford, U.K., 1970.

monochromator was used for energy selection and a Rh-coated mirror (set to an energy cutoff of 10 keV) was used for harmonic rejection. Internal energy calibration was performed by assigning the first inflection point of the Fe foil spectrum to 7111.2 eV. The solid samples were prepared by dilution in boron nitride, pressed into a pellet, and sealed between 38 μm Kapton tape windows in a 1 mm aluminum spacer. The solution samples were prepared by dilution in dichloromethane (~5 mM) and loaded into a Delrin Mössbauer/XAS sample holder, with a 6 μm polypropylene window. All samples were maintained at 10 K during data collection using an Oxford Instruments CF1208 continuous flow liquid helium cryostat. Solid and solution data were measured in transmission and fluorescence mode (using a Canberra Ge 30-element array detector), respectively.

XAS data were measured to $k = 15$ Å^{-1} for solid samples and $k = 11$ Å^{-1} for solution samples. The solution data range is truncated because of the highly absorbing nature of the solvent (dichloromethane), which made collection of higher k data prohibitive. Samples were monitored for photoreduction throughout the course of data collection. Only those scans which showed no evidence of photoreduction were used in the final average. The data represent 2, 9, 2, and 12 scan averages for the solid [LFeCl], solution [LFeCl], solid [LFe(η^2-NO$_3$)], and solution [LFe(η^2-NO$_3$)] complexes, respectively.

The data were calibrated and averaged using EXAFSPAK.[64] Pre-edge subtraction and splining were carried out using PYSPLINE.[65] A three-region cubic spline of order 2, 3, 3 was used to model the smooth background above the edge. Normalization of the data was achieved by subtraction of the spline and normalization of the post-edge region to 1. The resultant EXAFS was k^3-weighted to enhance the impact of high-k data.

Theoretical EXAFS signals $\chi(k)$ were calculated using FEFF (version 7.0)[66,67] and fit to the data using EXAFSPAK.[64] The nonstructural parameter E_0 was also allowed to vary but was restricted to a common value for every component in a given fit. The structural parameters varied during the refinements were the bond distance (R) and the bond variance (σ^2). The σ^2 is related to the Debye−Waller factor, which is a measure of thermal vibration and to static disorder of the absorbers/scatterers. Coordination numbers were systematically varied in the course of the analysis, but they were not allowed to vary within a given fit.

2.4. Computational Details. All calculations in this study were performed with the electronic structure program ORCA.[68] Single-point spin-unrestricted density functional calculations using the crystallographic coordinates were carried out with BP86 functional.[69–71] The expanded CP(PPP) basis set[72] was used for the iron atom, and all-electron polarized triple ξ (TZVP) Gaussian basis sets of the Alrichs group were used for all other atoms.[73] Calculations were carried out using the conductor-like screening model (COSMO) in an infinite dielectric.[74] While the calculations on [LFeCl] gave reasonable ground-state descriptions, the results of the calculations on [LFe(η^2-NO$_3$)], although converged, were physically unrealistic. This might be correlated to the observation that a geometry optimization on [LFeCl] results in a energy-minimized structure closely related to the solid structure, while geometry optimizations on [LFe(η^2-NO$_3$)] showed major structural rearrangements. For this reason, we refrain from further analysis of the [LFe(η^2-NO$_3$)] calculations.

3. Results and Analysis

3.1. Synthesis and Characterization. [LFe(η^2-NO$_3$)] was synthesized by reaction of H_2L with 1 equiv of $Fe(NO_3)_3 \cdot 9H_2O$ and 1.9 equiv of triethylamine in ethanol/acetone. The successful synthesis of the complex was confirmed by MS and FTIR (vide infra). Diffusion of n-pentane into a solution of [LFe(η^2-NO$_3$)] in t-butylmethyl ether yielded single-crystals suitable for X-ray diffraction. X-ray crystallography established the formulation as [LFe(η^2-NO$_3$)]$\cdot 0.5C_5H_{12}$. Because of loss of a fraction of pentane, the crystals were dried in high vacuum. FTIR spectra recorded before and after the high-vacuum treatment proved the identity of the sample. Elemental analysis showed that this sample, which was used for further measurements, was analytically pure [LFe(η^2-NO$_3$)]$\cdot 0.4C_5H_{12}$.

The reaction of the ligand H_2L with 1 equiv of $FeCl_3$ and 2 equiv of tetramethylammonium hydroxide in acetonitrile/methanol afforded blue [LFeCl] as confirmed by MALDI-TOF-MS and FTIR. However, a contamination with some fraction of the ligand H_2L became evident. The reaction conditions have been varied to avoid this contamination. For example, increasing the number of base equivalents yielded a mixture of H_2L, [LFeCl], and [LFe(μ_2-O)FeL]. All variations led either to the formation of other complexes and not to [LFeCl] or to a contamination with other complexes. Because of the similar solubilities of [LFeCl] and H_2L, it was not possible to separate H_2L completely from [LFeCl]. Even after several recrystallization steps, contaminations with H_2L remained. The sample used for further measurements was established by elemental analysis to be [LFeCl]$\cdot 0.09H_2L \cdot 0.07CHCl_3$.

The IR spectra of both [LFe(η^2-NO$_3$)] and [LFeCl] exhibit the characteristic features of the deprotonated ligand L^{2-}. The strong band at 810 cm^{-1} assigned to the ν_{as}(Fe−O−Fe) stretching mode in [LFe(μ_2-O)FeL][53] is not present in the IR spectra of [LFe(η^2-NO$_3$)] or [LFeCl]. The IR spectra of [LFe(η^2-NO$_3$)] and [LFeCl] measured as KBr pellets are nearly identical despite a strong band at 1520 cm^{-1} and a

(61) The program package MX was used for simulation of the Mössbauer spectra with applied magnetic fields by a full-matrix diagonalization approach of the appropriate spin-Hamiltonian. Bill, E. Unpublished work.
(62) Trautwein, A. X.; Bill, E.; Bominaar, E. L.; Winkler, H. *Struct. Bonding* **1991**, *78*, 1–95.
(63) Press, W. H.; Flannery, B. P.; Teukolsky, S. A.; Vettering, W. T. *Numerical Recipes*; Cambridge Unversity Press: Cambridge, U.K., 1990.
(64) George, G. N. *EXAFSPAK, Stanford Synchrotron Radiation Laboratory*; Stanford Linear Accelerator Center, Stanford University: Stanford, CA, 1996.
(65) Tenderholt, A. *PySpline, Stanford Synchrotron Radiation Laboratory*; Stanford Linear Accelerator Center, Stanford University: Stanford, CA, 2005.
(66) Mustre de Leon, J.; Rehr, J. J.; Zabinsky, S. I.; Albers, R. C. *Phys. Rev. B* **1991**, *44*, 4146–4156.
(67) Rehr, J. J.; Mustre de Leon, J.; Zabinsky, S. I.; Albers, R. C. *J. Am. Chem. Soc.* **1991**, *113*, 5135–5140.
(68) Neese, F. *ORCA: An ab Initio, Density Functional and Semiempirical Program Package*, version 2.6, revision 04; University of Bonn: Bonn, Germany, 2007.
(69) Becke, A. D. *Phys. Rev. A* **1988**, *38*, 3098–3100.
(70) Perdew, J. P. *Phys. Rev. B* **1986**, *33*, 8822–8824.
(71) Perdew, J. P. *Phys. Rev. B* **1986**, *34*, 7406–7406.
(72) Neese, F. *Inorg. Chim. Acta* **2002**, *337*, 181–192.
(73) Schafer, A.; Huber, C.; Ahlrichs, R. *J. Chem. Phys.* **1994**, *100*, 5829–5835.
(74) Klamt, A.; Schüürmann, G. *J. Chem. Soc., Perkin Trans. 2* **1993**, *2*, 799–805.

weaker band at 1385 cm^{-1} observed in the spectrum of [LFe(η^2-NO_3)]. The band at 1520 cm^{-1} corresponds to coordinated NO_3^-,[75] while the 1385 cm^{-1} band corresponds to uncoordinated NO_3^- indicating some substitution of NO_3^- by Br^- in the KBr pellet. Analogously, the FTIR spectrum of [LFe(η^2-NO_3)] measured in CH_2Cl_2 solution exhibits the band of coordinated NO_3^- at 1524 cm^{-1} and a weaker band at 1712 cm^{-1}. However, a new prominent band at 1356 cm^{-1} corresponds to free NO_3^- in CH_2Cl_2 solution.[76] The frequencies of the C−O stretching mode of the phenolates are found at 1265 and 1268 cm^{-1} in [LFe(η^2-NO_3)] and [LFeCl], respectively. They differ significantly from the corresponding frequencies for [LFe(μ_2-O)FeL] (1273 cm^{-1}) and for the free ligand H_2L (1234 cm^{-1}).

3.2. Crystal and Molecular Structures. The crystal structures of [LFe(η^2-NO_3)]·0.5C_5H_{12}, [LFeCl]·$CHCl_3$, and [LFeCl]·2CH_3CN were determined by single-crystal X-ray diffraction at 100, 183, and 100 K, respectively.

The crystal structure of [LFe(η^2-NO_3)]·0.5C_5H_{12} incorporates two independent molecules of [LFe(η^2-NO_3)] in the asymmetric unit. The molecular structures of these molecules exhibit no significant differences. Crystals of [LFeCl]·2CH_3CN were obtained after filtration of the reaction mixture and slow evaporation of the solvent. Recrystallization from chloroform/*n*-heptane lead to the formation of crystals of [LFeCl]·$CHCl_3$. The molecular structures of [LFeCl] in these two crystal structures exhibit only minor differences. Therefore, only the structure of [LFeCl] in crystals of [LFeCl]·$CHCl_3$ will be discussed in more detail.

Each structure contains neutral mononuclear complexes in which the 2-fold-deprotonated ligand L^{2-} coordinates a Fe^{III} ion using both *tert*-amines and both phenolates. The molecular structures of [LFe(η^2-NO_3)] and of [LFeCl] are displayed in Figure 1, and selected interatomic distances and angles are summarized in Tables 2 and 3.

In addition to the coordination by the ligand L^{2-}, the Fe^{III} ion in [LFe(η^2-NO_3)] is coordinated by a bidentate nitrate ion leading to a coordination number of six. The coordination polyhedron may be described by an octahedron that exhibits severe distortions mainly because of the small bite-angle of the nitrate ion of 59°. In contrast, the Fe^{III} ion in [LFeCl] is only five-coordinate by the ligand and one chloride ion resulting in a distorted square-pyramidal coordination polyhedron ($\tau = 0.31$).[77] The main difference in the molecular structures of [LFe(η^2-NO_3)] and [LFeCl] is the coordination conformation of the linear tetradentate ligand L^{2-}. Because of the bidentate nitrate ion occupying two positions cis to each other, the ligand in [LFe(η^2-NO_3)] adopts a β-cis conformation.[78] Interestingly, in [LFeCl], the donor atoms of ligand L^{2-} form the basal plane. Thus, the ligand adopts a trans conformation similar to the coordination in [LFe(μ_2-O)FeL].[53] The donor atoms of L^{2-} in [LFeCl] are placed between 0.16 and 0.17 Å from the best equatorial plane, while the iron atom is positioned above this plane by 0.51 Å. In [LFe(μ_2-O)FeL], the distance of the iron atoms from the equatorial plane is 0.58 Å.

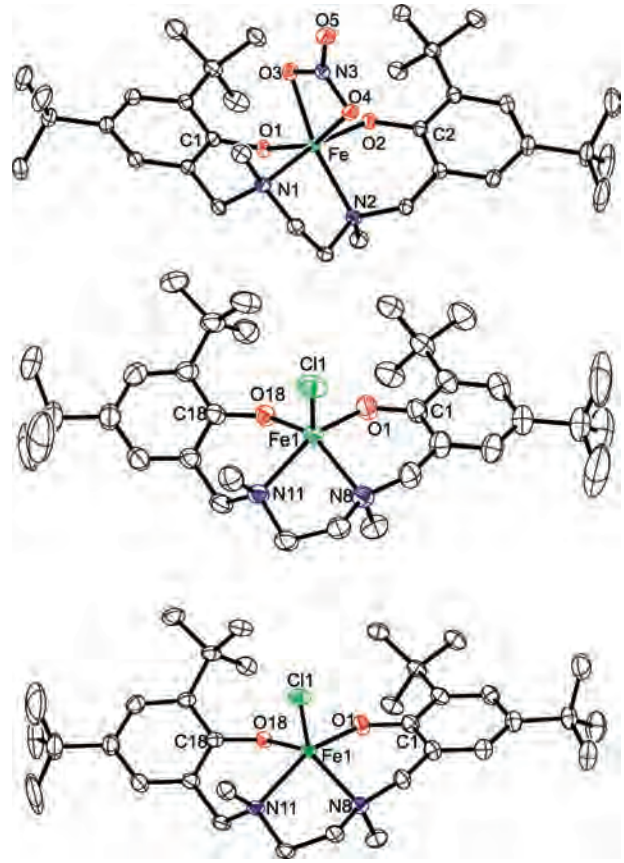

Figure 1. Molecular structures of [LFe(η^2-NO_3)] in crystals of [LFe(η^2-NO_3)]·0.5C_5H_{12} (top), [LFeCl] in crystals of [LFeCl]·$CHCl_3$ (middle), and [LFeCl] in crystals of [LFeCl]·2CH_3CN (bottom). Thermal ellipsoids are drawn at the 50% probability level; hydrogen atoms are omitted for clarity.

Table 2. Selected Interatomic Distances (Å) for [LFe(η^2-NO_3)]·0.5C_5H_{12}, [LFeCl]·$CHCl_3$, and [LFeCl]·2CH_3CN

	[LFe(η^2-NO_3)]·0.5C_5H_{12}		[LFeCl]·$CHCl_3$	[LFeCl]·2CH_3CN
Fe−O1	1.861(2)	Fe−O1	1.866(2)	1.864(2)
Fe−O2	1.850(2)	Fe−O18	1.855(2)	1.862(2)
Fe−N1	2.229(2)	Fe−N8	2.163(3)	2.162(2)
Fe−N2	2.153(2)	Fe−N11	2.284(3)	2.282(2)
Fe−O3	2.144(2)	Fe−Cl	2.2439(8)	2.248(1)
Fe−O4	2.236(2)			
N3−O3	1.278(2)			
N3−O4	1.282(2)			
N3−O5	1.218 (2)			
O1−C1	1.349(2)	O1−C1	1.339(4)	1.340(3)
O2−C2	1.342(2)	O18−C18	1.349(4)	1.346(2)

For [LFe(η^2-NO_3)], [LFeCl], and [LFe(μ_2-O)FeL],[53] all Fe−O^{Ph} bond lengths are approximately equal (between 1.85 and 1.87 Å). In contrast, the Fe−N bond distances exhibit large differences. In [LFe(η^2-NO_3)], the Fe−N bond distance trans to the Fe−O^{Ph} bond is 2.23 Å, while the Fe−N bond trans to the Fe−O^{NO_3} bond is at 2.15 Å. Interestingly, the lengths of the Fe−N bonds in [LFeCl], which are both in a trans-position to a Fe-phenolato bond, differ significantly (2.16 and 2.28 Å). The difference in the analogous bonds in

(75) Nakamoto, K. *Infrared and Raman Spectra of Inorganic and Coordination Compounds*, 5th ed., Part B; John Wiley & Sons: New York, 1997.
(76) Lever, A. B. P.; Mantovani, E.; Ramaswamy, B. S. *Can. J. Chem.* **1971**, *49*, 1957–1964.
(77) Addison, A. W.; Rao, T. N.; Reedijk, J.; van Rijn, J.; Verschoor, G. C. *J. Chem. Soc., Dalton Trans.* **1984**, 1349–1356.
(78) Selbin, J.; Bailar, J. C., Jr. *J. Am. Chem. Soc.* **1960**, *82*, 1524–1526.

Table 3. Selected Interatomic Angles (deg) for [LFe(η^2-NO_3)]·0.5C_5H_{12}, [LFeCl]·$CHCl_3$, and [LFeCl]·2CH_3CN

	[LFe(η^2-NO_3)]·0.5C_5H_{12}		[LFeCl]·$CHCl_3$	[LFeCl]·2CH_3CN
O1−Fe−O2	100.9(1)	O1−Fe−O18	94.78(8)	94.2(1)
O1−Fe−O3	95.8(1)	O1−Fe−N8	85.59(9)	85.2(1)
O1−Fe−O4	154.2(1)	O1−Fe−N11	158.03(9)	158.4(1)
O1−Fe−N1	91.5(1)	O1−Fe−Cl1	102.16(8)	102.6(1)
O1−Fe−N2	108.4(1)	O18−Fe−N8	139.57(9)	140.1(1)
O2−Fe−O3	96.0(1)	O18−Fe−N11	87.77(8)	88.1(1)
O2−Fe−O4	88.3(1)	O18−Fe−Cl1	112.56(7)	112.0(1)
O2−Fe−N1	165.2(1)	N8−Fe−N11	78.52(8)	79.5(1)
O2−Fe−N2	86.4(1)	N8−Fe−Cl1	106.79(6)	107.1(1)
O3−Fe−O4	59.1(1)	N11−Fe−Cl1	96.93(6)	96.4(1)
O3−Fe−N1	90.7(1)	Fe−O1−C1	136.1(2)	135.7(2)
O3−Fe−N2	154.9(1)	Fe−O18−C18	129.4(2)	128.5(2)
O4−Fe−N1	83.9(1)			
O4−Fe−N2	96.1(1)			
N1−Fe−N2	82.0(1)			
Fe−O1−C1	123.2(2)			
Fe−O2−C2	133.0(2)			

[LFe(μ_2-O)FeL] is remarkably smaller (2.21 and 2.24 Å).[53] The C−O bond lengths in [LFeCl], [LFe(η^2-NO_3)], and [LFe(μ_2-O)FeL] are between 1.34 and 1.35 Å, and therefore do not differ significantly.[53]

The Fe−O−C angles in the complex [LFe(η^2-NO_3)] are 123° and 133°, respectively. While the latter is in the typical range for Fe−O−C angles for phenol and phenolic derivatives (130° to 135°),[79] the former is significantly lower. The Fe−O−C angles in [LFeCl] are clearly larger (129° and 136°) than those in [LFe(η^2-NO_3)] and are only slightly out of the typical range.

3.3. Electronic Absorption Spectroscopy. UV−vis–NIR spectra of [LFeCl] and [LFe(η^2-NO_3)] were recorded in different solvents, namely, *n*-pentane, methanol, acetonitrile, and dichloromethane to obtain insight into the electronic structures of these complexes and their dependence on the solvents. The spectra are shown in Figure 2 and the spectroscopic properties are summarized in Table 4.

Each spectrum exhibits three main absorption bands in the range between 10 000 and 40 000 cm^{-1}. The high-energy band at approximately 35 600 cm^{-1} is also found in the spectrum of the free ligand H_2L (35 400 cm^{-1}) and can therefore be assigned to $\pi \rightarrow \pi^*$ transitions of the phenolic chromophores. In contrast, the two absorption bands at lower energies are absent in the spectrum of the free ligand and correspond, therefore, mainly to phenolate LMCT transitions. The bands around 29 600 cm^{-1} can be assigned to $p_\pi \rightarrow d_{\sigma^*}$ transitions, while the bands around 17 000 cm^{-1} can be assigned to $p_\pi \rightarrow d_{\pi^*}$ transitions.[53,79–82]

The absorption maxima and the shapes of the two low-energy bands change with the solvent, though less for the $p_\pi \rightarrow d_{\sigma^*}$ than for the $p_\pi \rightarrow d_{\pi^*}$ transitions. The strongest differences in the spectra of the two complexes are observed in the noncoordinating aprotic solvent *n*-pentane (Figure S1). While the energies of the $p_\pi \rightarrow d_{\sigma^*}$ transitions at 29 600 ± 100 cm^{-1} are quite similar, the $p_\pi \rightarrow d_{\pi^*}$ differ substantially: [LFe(η^2-NO_3)] 16400 cm^{-1} vs [LFeCl] 18200 cm^{-1}. On the other hand, the spectra of both complexes are nearly identical in the polar protic solvent methanol. This indicates that the solid-state structures (six-coordinate β-cis conformation vs five-coordinate trans conformation) are nearly retained in the aprotic nonpolar solvent *n*-pentane, while the complexes [LFe(η^2-NO_3)] and [LFeCl] convert to an almost identical species in the protic polar solvent methanol. The spectra measured in acetonitrile and dichloromethane are close to the one measured in *n*-pentane. This indicates that the molecular structures in these solvents are almost identical to those in *n*-pentane. EPR spectroscopy corroborates this result (vide infra).

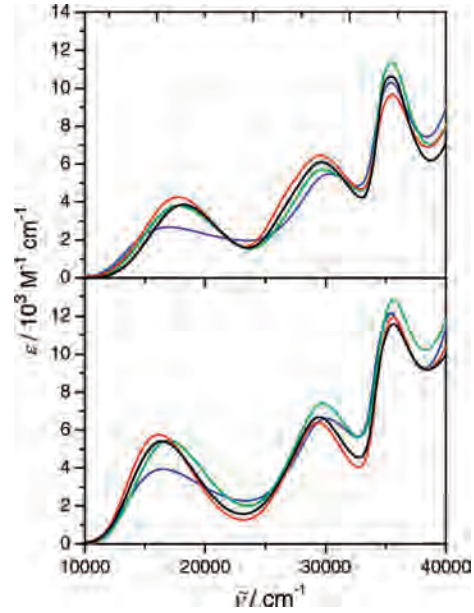

Figure 2. Electronic absorption spectra of [LFeCl] (top) and of [LFe(η^2-NO_3)] (bottom) at 25 °C (black, *n*-pentane; blue, methanol; green, acetonitrile; red, dichloromethane).

Table 4. Spectroscopic Properties of [LFe(η^2-NO_3)] and [LFeCl] at 25 °C in Different Solvents, $\tilde{\nu}$ (cm^{-1})/ε (M^{-1} cm^{-1})

[LFe(η^2-NO_3)] in			
methanol	16 400/3900	30 000/6600	35 300/12 100
acetonitrile	17 100/5400	29 800/7400	35 700/12 800
dichloromethane	16 100/5700	29 300/6400	35 600/11 900
n-pentane	16 400/5400	29 500/6700	35 600/11 600
[LFeCl] in			
methanol	16 700/2700	30 200/5500	35 500/10 300
acetonitrile	18 000/3800	29 800/5700	35 500/11 300
dichloromethane	17 500/4300	29 600/6200	35 300/12 200
n-pentane	18 200/3900	29 700/6100	35 500/10 600

3.4. Magnetic Susceptibility. [LFe(η^2-NO_3)]. Temperature-dependent magnetic susceptibility measurements of [LFe(η^2-NO_3)] display a constant effective magnetic moment of 5.87 μ_B at temperatures above 40 K (Figure 3a), which is close to the spin-only value of 5.92 μ_B for $S = 5/2$ as expected for an Fe^{III} high-spin complex. The effective moment decreases for lower temperatures and reaches 3.94 μ_B at 2 K because of the combined effects of field saturation, zero-field splitting, and antiferromagnetic intermolecular interactions. A spin-Hamiltonian simulation of the low-

(79) Davis, M. I.; Orville, A. M.; Neese, F.; Zaleski, J. M.; Lipscomb, J. D.; Solomon, E. I. *J. Am. Chem. Soc.* **2002**, *124*, 602–614.
(80) Karpishin, T. B.; Gebhard, M. S.; Solomon, E. I.; Raymond, K. N. *J. Am. Chem. Soc.* **1991**, *113*, 2977–2984.
(81) Schnepf, R.; Sokolowski, A.; Müller, J.; Bachler, V.; Wieghardt, K.; Hildebrandt, P. *J. Am. Chem. Soc.* **1998**, *120*, 2352–2364.
(82) Glaser, T.; Lügger, T. *Inorg. Chim. Acta* **2002**, *337*, 103–112.

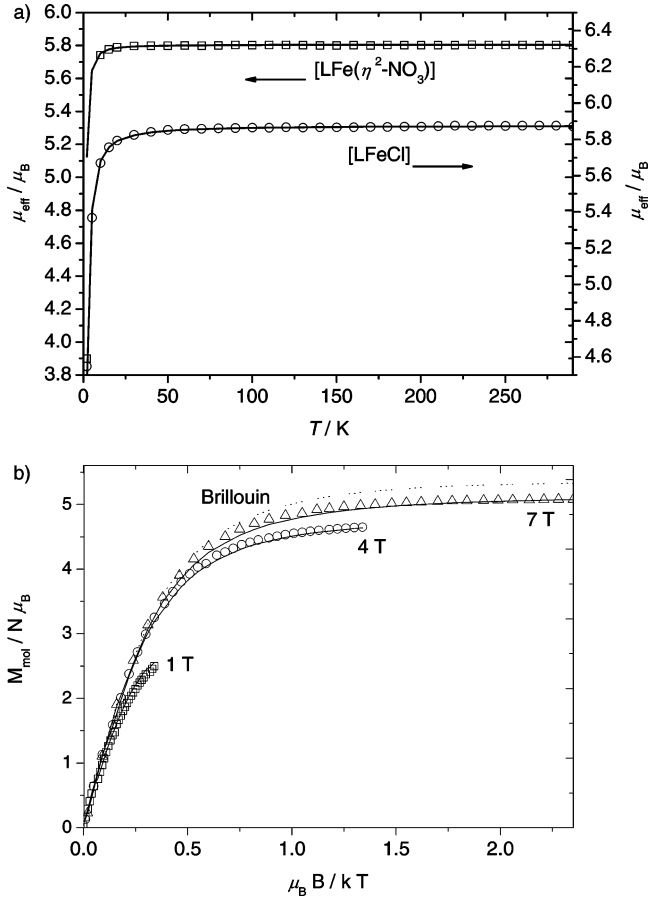

Figure 3. (a) Temperature-dependence of the effective magnetic moment, μ_{eff}, of solid [LFe(η^2-NO$_3$)] (top) and solid [LFeCl] (bottom) at 1 T. The solid lines are the fits to the experimental data using the spin Hamiltonian in eq 1 with $|D| = 1.2$ cm^{-1}, $E/D = 0.33$, and $g = 1.98$ and with $D = 1.15$ cm^{-1}, $E/D = 0.175$, $g = 1.987$, and $\theta_w = -0.5$ K for [LFe(η^2-NO$_3$] and [LFeCl], respectively. (b) Variable-temperature multiple-field (VTMF) magnetization measurements of solid [LFeCl] with an applied field of 1 (squares), 4 (circles), and 7 T (triangles). The solid lines are fits to the experimental data using the spin-Hamiltonian in eq 1 with $D = 1.15$ cm^{-1}, $E/D = 0.175$, $g = 1.988$, and $\theta_w = -0.48$ K. The dashed line is the Brillouin function for $S = 5/2$ with $g = 1.988$.

temperature magnetic properties based on eq 1 with $S = 5/2$ yields best results for a zero-field splitting parameter of $|D| = 1.2$ cm^{-1}, with $E/D = 0.33$ taken from the EPR data given below (solid line in Figure 3a). The electronic g value was found to be $g = 1.98$, according to the high-temperature plateau of the experimental data. Its value is reasonably close to $g = 2$ expected for the ^6S state of Fe^{III} high-spin. Alternatively to the zero-field splitting D, a Weiss-constant θ_w was introduced in the calculations to account for intermolecular interactions, which have been observed experimentally by EPR spectroscopy. However, the obtained value of -0.08 K is an upper (negative) limit for θ_w. Simulations with lower $|\theta_w|$ and D values lower than 1.2 cm^{-1} are virtually indistinguishable from the results using either $\theta_w = -0.08$ K or $|D| = 1.2$ cm^{-1}. Note that the sign of D is immaterial in this case because of the limiting value of E/D.

[LFeCl]. The microcrystalline sample of [LFeCl] contained some contamination of the free ligand, so that the values of μ_{eff} are given with respect to an effective molar mass of $M = 669.71$ g/mol, which corresponds to the sample composition [LFeCl]·0.09H$_2$L·0.07CHCl$_3$ obtained by elemental analysis (vide supra). Without this correction the molar magnetic moment would be significantly underestimated. The magnetic properties of [LFeCl] closely resemble those of [LFe(η^2-NO$_3$)], showing a temperature-independent effective magnetic moment of 5.87 μ_B above 50 K and a similar low-temperature drop to 4.55 μ_B at 2 K (Figure 3a). The temperature dependence of the susceptibility data could be well simulated by using $S = 5/2$ and the parameters $D = 1.15$ cm^{-1}, $E/D = 0.175$ (taken from EPR), $g = 1.987$, and a Weiss constant of $\theta_w = -0.5$ K.

The chloride complex was investigated in more detail by variable-temperature magnetization measurements at multiple fields of 1, 4, and 7 T with data sampling on the $1/T$ scale. The technique (VTMF) yields a high density of data points at temperatures between 2 and 6 K and provides a rather independent examination of the zero-field splitting parameter. The information is derived from the increasing competition of the zero-field and the Zeeman interaction at the different fields.[83] This leads to a pronounced nesting behavior of the different iso-field data sets if zero-field splitting is present, as is also observed for [LFeCl] (see Figure 3b). All curves differ also from the Brillouin function for an isotropic spin system without zero-field splitting (dashed line in Figure 3b). Eventually also intermolecular spin coupling may be revealed from VTMF data, because the nesting behavior of the iso-field curves is affected by θ_w in a different manner than by zero-field interaction.

Corresponding global spin-Hamiltonian simulations for the VTMF data from [LFeCl] with automatic parameter optimization yield $D = +1.15 \pm 0.10$ cm^{-1}, $g = 1.988 \pm 0.002$ (mostly determined from the high-temperature plateau of $\mu_{eff}(T)$ shown in Figure 3a), and a Weiss constant of $\theta_w = -0.48 \pm 0.05$ K. The rhombicity parameter was fixed to $E/D = 0.175$, according to the EPR data. In summary, an excellent global fit was obtained (lines in Figure 3b), and the parameters are in good agreement with the magnetic Mössbauer and EPR investigations given below. Only the sign of D had to be taken from the other techniques because a similar or even marginally better fit of the magnetization curves is possible with a negative D parameter.[84] But that may be expected for a powder sample of a complex with such a "weak" zero-field interaction. The presence of intermolecular interactions, however, with θ_w of about -0.5 K is significant because the correct nesting of the 1, 4, and 7 T iso-field curves can not be obtained from fits without finite values for θ_w.

3.5. EPR Spectroscopy. [LFe(η^2-NO$_3$)]. Figure 4 displays the X-band EPR derivative spectra of [LFe(η^2-NO$_3$)] dissolved in methanol, butyronitrile, ethyl acetate, and dichloromethane at temperatures in the range of 4−14 K. The

(83) Girerd, J.-J.; Journaux, Y. In *Physical Methods in Bioinorganic Chemistry*; Que, L., Jr., Ed.; University Science Books: Sausalito, CA, 2000.

(84) The best values for fits of the magnetic data with negative zero-field splitting are $D = -1.00 \pm 0.10$ cm^{-1}, with $E/D = 0.175$ (from EPR), $g = 1.988 \pm 0.002$, and $\theta_w = -0.50 \pm 0.05$ K. The solution, however, could be ruled out from the other data, mostly the analysis of EPR spectra from frozen solutions, which yield more "microscopic" magnetic information and for which intermolecular spin coupling is much less significant.

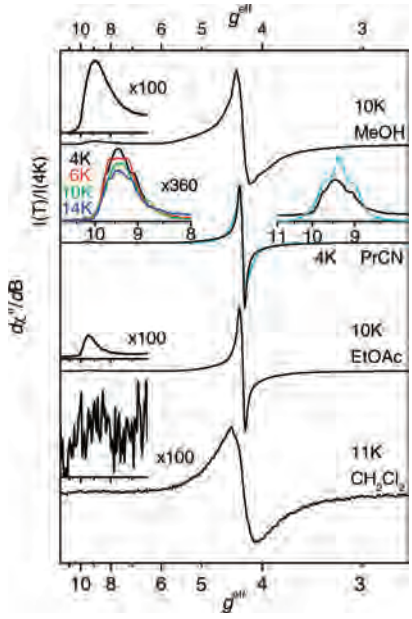

Figure 4. X-band EPR spectra of [LFe(η^2-NO_3)] measured in frozen methanol (MeOH, 10 K), butyronitrile (PrCN, 4, 6, 10, and 14 K), ethyl acetate (EtOAc 10 K), dichloromethane (CH_2Cl_2, 10 K), and simulation of the spectrum measured in butyronitrile at 4 K (light blue). The enlarged signals at $g^{eff} \approx 9$ are displayed in the insets. The inset in the spectrum measured in butyronitrile (left) presents the temperature dependence of the signal at $g = 9.44$. The intensities in this inset are normalized to the intensities of the signal at $g = 4.3$ at the respective temperature: $I(T)/I(4\ K) = I(T, g = 4.3)/I(4\ K, g = 4.3)$; $I(T, g = 4.3)$; intensity at $g = 4.3$ at temperature T. The field axes have been converted to a common g axis for direct comparison. Parameters for the simulation of the signal at $g = 4.3$: $g_{zz} = g_{xx} = g_{yy} = 2.00$, $D = 1.3\ cm^{-1}$, and $E/D = 0.327$. For the simulation of the signal at $g = 9.44$, a hyperfine coupling to two hydrogen atoms ($I = 1/2$) with $A = 25 \times 10^{-4}\ cm^{-1}$ was taken into account. [Experimental conditions: $\nu = 9.4313$, 9.4305, 9.4316, 9.6343 GHz; microwave power = 100.3, 10.0, 50.4, 50.5 μW; field modulation = 2.0, 1.0, 2.0, 0.75 mT, respectively.]

spectra depend strongly on the nature of the solvent, but they all show a persistent derivative signal at $g = 4.3$ and a weak positive low-field peak at about $g \approx 9$. These are typical features of an $S = 5/2$ spin system with large rhombicity ($E/D \approx 0.33$) and "strong" zero-field splitting (i.e., $D \gg h\nu \approx 0.3\ cm^{-1}$ at X-band). This interaction splits the $S = 5/2$ ground-state of the iron atom into three well-isolated Kramers doublets separated by 3.5 D, so that X-band EPR transitions can occur only within doublets. In this case, the dominant $g = 4.3$ signal arises from the magnetically isotropic middle doublet ($g_{xx}^{eff} = g_{yy}^{eff} = g_{zz}^{eff}$), whereas the peak at $g \approx 9$ owes its origin to transitions within the very anisotropic lower Kramers doublet along g_{yy}^{eff} and to the g_{xx}^{eff} transitions of the upper doublet.[62,85] For $E/D \approx 0.33$, the sign of D is without physical meaning, since the lower and the upper doublets have the same magnetic anisotropy, just along different main axes.

The prominent $g = 4.3$ signal is rather narrow and has a reasonable line shape for [LFe(η^2-NO_3)] dissolved in butyronitrile and in ethyl acetate (Figure 4), but it is severely broadened for other solvents (Figure 4, MeOH, and dichloromethane). More difficult to understand, however, is a shift of the effective g value for the weak low-field peak, which is dependent on the solvent used. For butyronitrile, the g_{yy}^{eff} peak appears at $g = 9.44$ but changes also to 9.35 (ethyl acetate), 8.90 (methanol), and ~8.9 (dichloromethane), respectively. Actually, all the values are slightly lower than what is expected for $E/D \approx 0.3$, and what one can read off the rhombogram for the presence of an unsplit $g = 4.3$ signal. (This is further substantiated by the simulation given in the next paragraph.) Therefore we have to assume that the spectra from all four solvents first are more or less perturbed by a poor glass which yields heterogeneous line broadening of some parts of the spectrum. (Butyronitrile affords the best glassing medium of the solvents used.) But sizable intermolecular interactions must be present[86] because the g shifts of the low-field peaks toward $g = 2$ are most probably caused by the effect of exchange narrowing.[87] This means that clustering of the neutral complex molecules would occur in the frozen solutions, even in dilute samples.

The spectrum of [LFe(η^2-NO_3)] dissolved in butyronitrile could be reasonably well simulated by using the spin Hamiltonian for $S = 5/2$ (eq 1) with parameters $D = 1.3\ cm^{-1}$, $E/D = 0.327$, and $g = 2.0$, except for a stark misfit of the low-field peak appearing at $g = 9.61$, in contrast to the experimental signal at $g = 9.44$. Lowering the rhombicity would in fact improve that part of the fit (about $E/D \approx 0.21$), but the corresponding solutions yield unacceptably large splitting of the $g = 4.3$ main signal (i.e., for the effective g values of the middle Kramers doublet). We have also examined the effects of higher-order terms[88] in the spin Hamiltonian (O_4), which are usually neglected unless quasi-cubic ligand symmetry prevails. However, these terms also failed to improve the simulation. Thus, we refrain from more sophisticated approaches, presuming that the central part of the spectrum at $g \approx 4.3$ is the most meaningful feature and that the low-field peaks are not readily simulated because of perturbations caused by sample clustering. The position, shape, and width of the strong unsplit $g = 4.3$ signal clearly renders the rhombicity close to $E/D = 0.3$ (actually, we find 0.327 ± 0.03). For the final simulation, we adopted Lorentzian line shapes for the spin-packets in the powder summation with frequency-constant line widths $\Gamma_\nu = 20$ mT (increases with field strength, value given for $g = 1$). To reproduce the overall broad shape of the spectrum, a Gaussian distribution of the rhombicity parameter had to be invoked with $\sigma(E/D) = 0.05$ (full width at half-maximum).

The value of the axial zero-field splitting parameter could be estimated from a fit of the intensity ratio of the $g = 4.3$ peak and the low-field peak measured at 4, 6, 10, and 14 K. The procedure is not highly accurate because the simulations do not match the line shape of the derivative peaks very well, and the absorptions of the anisotropic lowest Kramers doublet cannot be readily derived from the derivative spectra because they extend from $g^{eff} = 9.61$ to high fields beyond $g^{eff} = 0.6$ and the exact shape of the powder subspectrum also depends

(85) Hagen, W. R. *Adv. Inorg. Chem.* **1992**, *38*, 165–222.

(86) Kennedy, B. J.; Brain, G.; Horn, E.; Murray, K. S.; Snow, M. R. *Inorg. Chem.* **1985**, *24*, 1647–1653.

(87) Bencini, A.; Gatteschi, D. *Electron Paramagnetic Resonance of Exchanged Coupled Systems*; Springer-Verlag; Berlin, 1990.

(88) Simaan, A. J.; Banse, F.; Girerd, J. J.; Wieghardt, K.; Bill, E. *Inorg. Chem.* **2001**, *40*, 6538–6540.

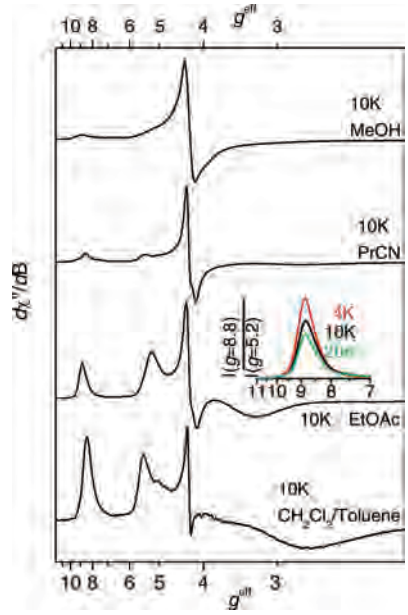

Figure 5. X-band EPR spectra of [LFeCl] recorded in frozen methanol (MeOH, 10 K), butyronitrile (PrCN, 10 K), ethyl acetate (EtOAc, 4, 10, 20 K), and dichloromethane/toluene (CH_2Cl_2/Tol, 10 K). The inset in the spectrum measured in butyronitrile presents the temperature-dependence of the signal at $g = 8.8$. The intensities in this inset are normalized to the intensities of the signal at $g = 5.2$ at the respective temperature: $I(g = 8.8)/I(g = 5.2)$. The field axes have been converted to a common g axis for direct comparison. [Experimental conditions: $\nu = 9.4280$, 9.4290, 9.4314, 9.4339 GHz; microwave power = 100.6, 50.3, 50.4, 100.3 μW; field modulation = 2.0, 2.0, 2.0, 1.5 mT, respectively.]

on D. But the trend in the amplitude of the simulated derivative peaks as a function of temperature allows a rough estimate, $D = 1.1 \pm 0.2$ cm^{-1}, which fits well to the magnetization data obtained for the solid. This value is in nice agreement with the rhombic EPR signal of 3,4-PCD.[89]

Interestingly, the low-field signal at $g = 9.44$ in the spectrum of [LFe(η^2-NO_3)] dissolved in butyronitrile exhibits a triplet hyperfine splitting with a hyperfine coupling constant of about 25×10^{-4} cm^{-1}. As the pattern seems to indicate the presence of two quasi-equivalent protons that couple to the iron spin, this was taken into account by two $I = 1/2$ nuclei. It must be noted that this hyperfine coupling represents only one component of the full hyperfine coupling tensor. The other components are not resolved. The value of the isotropic hyperfine coupling constant is thus smaller than 25×10^{-4} cm^{-1}.

[LFeCl]. The chloride complex dissolved in methanol and butyronitrile also shows virtually rhombic X-band EPR spectra at 10 K (Figure 5, MeOH and PrCN), similar to those of [LFe(η^2-NO_3)] in the same solvents. The shape of the strong $g = 4.3$ signal, and the appearance of the low-field peak also depends on the solvent, with a slightly more pronounced effect than was observed for [LFe(η^2-NO_3)]. In butyronitrile solution moreover, the complex shows a small, but distinct, splitting of the $g = 4.3$ signal and an additional weak extra line at $g = 5.4$. For the noncoordinating solvents, ethyl acetate (Figure 5, EtOAc) and dichloromethane/toluene mixture (Figure 5, CH_2Cl_2/toluene), however, the spectra are

(89) Whittaker, J. W.; Lipscomb, J. D.; Kent, T. A.; Münck, E. *J. Biol. Chem.* **1984**, *259*, 4476–4486.

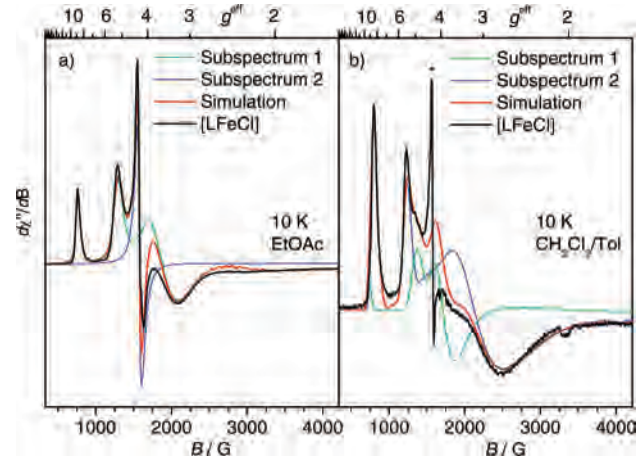

Figure 6. X-band EPR spectra of [LFeCl] in frozen ethyl acetate (a) and dichloromethane/toluene (b) at 10 K as shown in Figure 5 and simulations of the spectra. The parameters for the simulation of the spectrum measured in ethyl acetate are: subspectrum 1 (88%): $g_{xx} = g_{yy} = 1.98$, $g_{zz} = 2.005$, $D = 2.1$ cm^{-1}, and $E/D = 0.175$; Gaussian distribution of E/D: $\sigma(E/D) = 0.03$, $\Gamma_v = 35$ mT (at $g = 1$). For subspectrum 2 (12%): simple powder simulation with effective spin $S^{eff} = 1/2$, $g_x^{eff} = 4.20$, $g_y^{eff} = 4.27$, and $g_z^{eff} = 4.29$. The parameters for the simulation of the spectrum measured in dichloromethane/toluene are as follows: subspectrum 1 (85%) $g_{xx} = g_{yy} = g_{zz} = 2.00$, $D \approx 1.0$ cm^{-1}, and $E/D \approx 0.13$; Gaussian distribution of E/D: $\sigma(E/D) = 0.03$; subspectrum 2 (15% relative intensity) $g_{xx} = g_{yy} = g_{zz} = 2.00$, $D \approx 1.0$ cm^{-1}, and $E/D = 0.21$; Gaussian distribution of E/D: $\sigma(E/D) = 0.03$. Asterisk (*) represents a minor species of <5%, which is a full rhombic $S = 5/2$ species.

significantly different and clearly show the presence of a major species with lower rhombicity than $E/D = 0.33$. That is inferred from the strong, positive low-field peaks at about $g \approx 8.5$ and 5.4. (The latter is similar to that mentioned for butyronitrile.) In addition, there is a broad, negative trough in the range at $g = 3.5-2.5$, and the maximum of the absorption (zero-crossing in the derivative spectrum) is at g values below $g = 4$. A rhombic species centered at $g = 4.3$ is also present but only with very minor intensity. All spectra shown in Figure 5 are broad, indicating microheterogeneity and presumably also some degree of intermolecular spin−spin interactions for the four different solvents.

The spectrum of [LFeCl] in ethyl acetate could be nicely simulated with the assumption of two subspectra, both with $S = 5/2$ but different rhombicity (Figure 6a). The major contribution (subspectrum 1, ~88% integrated intensity) has the parameters $g_{xx} = g_{yy} = 1.98$, $g_{zz} = 2.005$, $D = 2.1$ (± 0.5) cm^{-1}, and $E/D = 0.175(\pm 0.005)$, and accounts for the lines at $g^{eff} = 8.83$, 5.2, 4.3, and 3.2. For a correct simulation of the overall broad shape of the subspectrum, a Gaussian distribution of E/D had to be invoked with $\sigma(E/D) = 0.03$ and intrinsic line widths of the spin packets $\Gamma_v = 35$ mT (at $g = 1$). The second subspectrum (subspectrum 2) in the simulation for [LFeCl] in ethyl acetate was achieved by a simple powder simulation for an effective spin $S^{eff} = 1/2$ with effective g values: $g_{xx}^{eff} = 4.20$, $g_{yy}^{eff} = 4.27$, and $g_{zz}^{eff} = 4.29$ (relative intensity 12%).

The positive sign of D for the major subspectrum 1 of [LFeCl] in ethyl acetate is significant and can be clearly inferred from the relative intensity of the signal at $g = 8.83$, which arises from the $|m_S = \pm 1/2\rangle$ Kramers doublet. The

persistently high intensity of the signal particularly at 4 K reveals ground-state origin because of a positive D value (Figure 5 inset). At elevated temperatures of 10 and 20 K the intensity of that line fades relative to the other peaks, according to the thermal depopulation with rising temperature.

In CH_2Cl_2/toluene mixture the chloride complex again exhibits four EPR signals like in ethyl acetate solution and with similar g values at $g^{eff} = 8.4$, 5.5, 4.3 and 2.7. However, the features around $g^{eff} = 4.3$ are more detailed, and for a good simulation, two subspectra had to be introduced for the intense major absorptions (here the sharp rhombic peak itself at $g = 4.3$ was even completely ignored because of vanishing total intensity <5% in the corresponding narrow absorption line). The spin Hamiltonian parameters obtained from optimization are $g_{xx} = g_{yy} = g_{zz} = 2.00$, $D \approx 1.0$ (± 0.5) cm^{-1}, and $E/D \approx 0.13$ (± 0.02) for subspectrum 1 (85% relative intensity) and $g_{xx} = g_{yy} = g_{zz} = 2.00$ and $E/D = 0.21$ (± 0.01) for subspectrum 2 (15% intensity, $|D|$ is larger than 0.4 cm^{-1}, but could not be further specified due to the weak intensity of this subspectrum) (Figure 6b). The simulations for both subspectra 1 and 2 are less sensitive to changes in D but highly sensitive to changes in E/D. The actual shapes of the spectra were achieved with Gaussian distribution of the rhombicity parameters according to $\sigma(E/D) = 0.03$ for both subspectra.

In summary, the EPR measurements of the chloride complex [LFeCl] reveals Fe^{III} high-spin, $S = 5/2$, with distinct, medium-strong rhombicity $E/D = 0.13-0.175$ in noncoordinating solvents. The axial zero-field splitting parameter is positive for the complex in the solutions but slightly higher than the value derived from magnetic susceptibility measurements on solid material ($D = 2.1 \pm 0.5$ cm^{-1} in ethyl acetate and $D = 1.0 - 1.5$ cm^{-1} in CH_2Cl_2/toluene mixture versus $D = +1.15 \pm 0.10$ cm^{-1} in the solid). In the coordinating solvents methanol and butyronitrile, the EPR spectra are significantly different, apparently because of major changes in the coordination sphere of the iron atom.

3.6. Mössbauer Spectroscopy. Zero-field Mössbauer spectra of the chloride complex [LFeCl] measured at 80 and 297 K display only very asymmetrically broadened asymmetric line doublets as shown in Figure 7, virtually independent of the temperature. The apparent line broadening is typical of paramagnetic relaxation with intermediate rates up to room temperature. This is not unusual for high-spin Fe^{III}, particularly for small molecules because their spin−orbit−lattice relaxation (with relaxation time T_1) can be rather slow because of a vanishing orbital moment. Then the total spin relaxation time is determined by intermolecular spin−spin processes with relaxation times T_2 that show essentially no temperature dependence. We performed a phenomenological fit of the zero-field spectrum at 80 K of [LFeCl] with an asymmetric Lorentzian quadrupole doublet (intensity ratio 1.25:1 and line widths 0.63:1) that yields preliminary values for the isomer shift and the quadrupole splitting of $\delta = 0.49$ mm/s and $|\Delta E_Q| = 1.36$ mm/s (for better values see magnetic spectra below). The Mössbauer spectrum of [LFe(η^2-NO_3)] is broader than that of [LFeCl], so we refrained from further analyses.

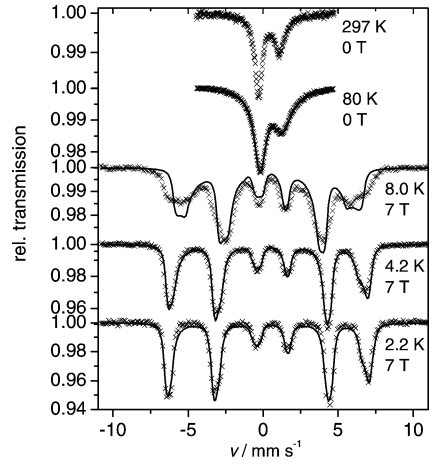

Figure 7. Zero-field Mössbauer spectra of solid [LFeCl] recorded at 80 and 297 K and magnetic Mössbauer spectra of solid [LFeCl] recorded at 2.2, 4.2, and 8 K with a field of 7 T applied perpendicular to the γ-rays. The solid line in the zero-field Mössbauer spectrum recorded at 80 K is a phenomenological fit with an asymmetric Lorentzian quadrupole doublet (intensity ratio 1.25:1 and line widths 0.63:1), an isomer shift $\delta = 0.49$ mm/s, and the quadrupole splitting $|\Delta E_Q| = 1.36$ mm/s. The solid lines in the spectra recorded with an applied field are spin Hamiltonian simulations in the limit of fast spin relaxation with parameters $D = +2.2$ cm^{-1} and $E/D = 0.175$, $g = 2.0$ (isotropic), $\delta = 0.47$ mm/s, $\Delta E_Q = 1.24$ mm/s, $\eta = 0.37$ (with Euler angels $\alpha = 124°$, $\beta = 148°$), $\mathbf{A}/g_N\beta_N = (-19.51, -19.49, -18.50)$ T. The spectrum measured at 8 K and 7 T was not considered for the parameter optimization because of apparent relaxation broadening.

Magnetic Mössbauer spectra of the chloride complex [LFeCl] were measured from powder material at liquid helium temperatures with applied fields of 4 and 7 T. As shown in Figure 7, the spectra display rather well-resolved magnetic hyperfine patterns at 7 T and 2.2 or 4.2 K. At higher temperatures and lower field, the spectra show excessive broadening by spin relaxation effects, and have therefore not been analyzed further. The large overall splitting of the resolved spectra indicates the presence of strong internal fields of about 48 T that are rather typical of Fe^{III} h.s. The spectra could be readily simulated by using zero-field splitting parameters $D = +2.2$ (± 0.1) cm^{-1} and $E/D = 0.175$ as applied above for the EPR simulations for the ethyl acetate solution. The appearance of the resolved lines with a clear quadrupole shift (of the inner four lines against the outer two), partial anisotropic broadening, and a distinct intensity pattern is typical of an anisotropic ground state. For $S = 5/2$ with positive D value, this is the Kramers doublet $|m_S = \pm 1/2>$ with $\mathbf{g}^{eff} \approx (2.2, 8.8, 1.3)$. However, a rather similar fit could be obtained also with negative D values, $D = -1$ cm^{-1}, $E/D = 0.16$ (ground state $|m_S = \pm 5/2>$ with $\mathbf{g}^{eff} \approx (0.2, 0.3, 9.9)$. Mostly the electric field gradient had to be rotated for this alternative by about 90° around the x-axis because of the different easy axis of magnetization. Therefore the actual choice of a positive D value can only be based on the EPR results given above. Moreover, we realized that lower positive D values which were determined from the VTMF magnetization measurement of solid [LFeCl] ($D = +1.15 \pm 0.10$ cm^{-1}), are not consistent with the simulation of the magnetic Mössbauer spectra. Because a more sophisticated approach was applied for the analysis of the magnetization data with explicit consideration of intermolecular interaction, which are neglected in the Mössbauer simula-

Table 5. Results of Calculations for the Five Metal d-Based Orbitals in [LFeCl]

MO	163	164	165	166	167	total
energy/eV	−3.60	−3.33	−3.07	−2.89	−1.86	
label	d_π^{ax}	$d_\pi^{eq\ 1}$	$d_\pi^{eq\ 2}$	d_σ^{ax}	d_σ^{eq}	
orbital contribution						
d_{z^2} (%)	1.8		5.8	56.7	2.5	
$d_{x^2-y^2}$ (%)	15.3	30.7	32.7	1.3		
d_{xy} (%)		1.5		1.8	62.4	
d_{xz} (%)		41.1	30.8	3.4	1.4	
d_{yz} (%)	58.7	4.1		6.9		
Fe 3d total (%)	75.9	77.4	74.1	70.1	66.4	363.9
Fe 4p	1.1	0.7	1.7	1.8	0.8	6.1
O^{Ph} (%)	2.7	9.3	11.9	7.4	8.4	39.7
N (%)	0.8	1.3	1.4	2.7	10.6	16.8
remaining L^{2-}	12.3	5.9	4.2	7	8.9	38.3
Cl (%)	4.5	2.8	3.3	7.7	0.7	19

tions, we suggest that the magnetization result yields a better value for the intrinsic electronic properties of Fe^{III} in solid [LFeCl].

The electric field gradient for [LFeCl] is found to be positive from the magnetic Mössbauer spectra, according to a quadrupole splitting of $\Delta E_Q = +1.24 \pm 0.20$ mm/s and a asymmetry parameter $\eta = 0.4$. The tensor axes are rotated against the principal axes of the zero-field interaction by the Euler angles $\alpha = 124(\pm 20)°$, $\beta = 148(\pm 20)°$. The isomer shift is $\delta = 0.47 \pm 0.02$ mm/s, which is readily consistent with high spin Fe^{III}, in contrast to the remarkably large quadrupole splitting. The latter indicates rather strong asymmetry in the covalency of the ligands, somewhat similar to what is encountered in oxo-bridged diferric species, which show even larger electric quadrupole coupling. The magnetic hyperfine tensor for the complex is $\mathbf{A}/g_N\beta_N = (-19.51 \pm 0.1, -19.49 \pm 0.1, -18.50 \pm 0.1)$ T. The isotropic part $A_0/g_N\beta_N = 19.2$ T is lower than the limit of 22 T invoked for a ionic complex, which again reveals covalency of the ligands. Also the anisotropy of **A** is remarkable for an S-state ion.

3.7. Electronic Structure Calculations. Ground state DFT calculations on [LFeCl] have been used to obtain electronic structure descriptions, in particular the σ- and π-covalencies of the Fe−O^{Ph} bonds. The orbital compositions for the metal-based d-orbitals are summarized in Table 5 and the spin-down metal-based molecular orbitals, together with the coordinate system, are shown in Figure 8.

For [LFeCl], the d_{yz} orbital (MO 163) is lowest in energy and is dominated by a π-bonding interaction with the $3p_y$ orbital of the axial Cl^- ligand. MOs 164 and 165 correspond to symmetry adapted mixings of the d_{xz} and $d_{x^2-y^2}$ orbitals and are dominated by π-interactions with the oxygen $2p_y$ orbitals of the phenolates (note that the approximate C_s symmetry with the mirror plane bisecting the O^{Ph}−Fe−O^{Ph} and N−Fe−N angles leads to a 45° rotation of the "usual" choice for the coordinate system with the axes pointing to the ligands). MO 166 is a metal d_{z^2} orbital, with ~8% Cl $3p_z$ contribution, and a significant O $2p_z$ contribution from the phenolates. The d_{xy} (MO 167) is the highest in energy and shows strong σ-antibonding interactions from both the phenolates and the amines. There is a total of ~6% 4p mixing into the five metal d-based orbitals consistent with the intense pre-edge feature which is observed at the Fe K-edge (vide infra).

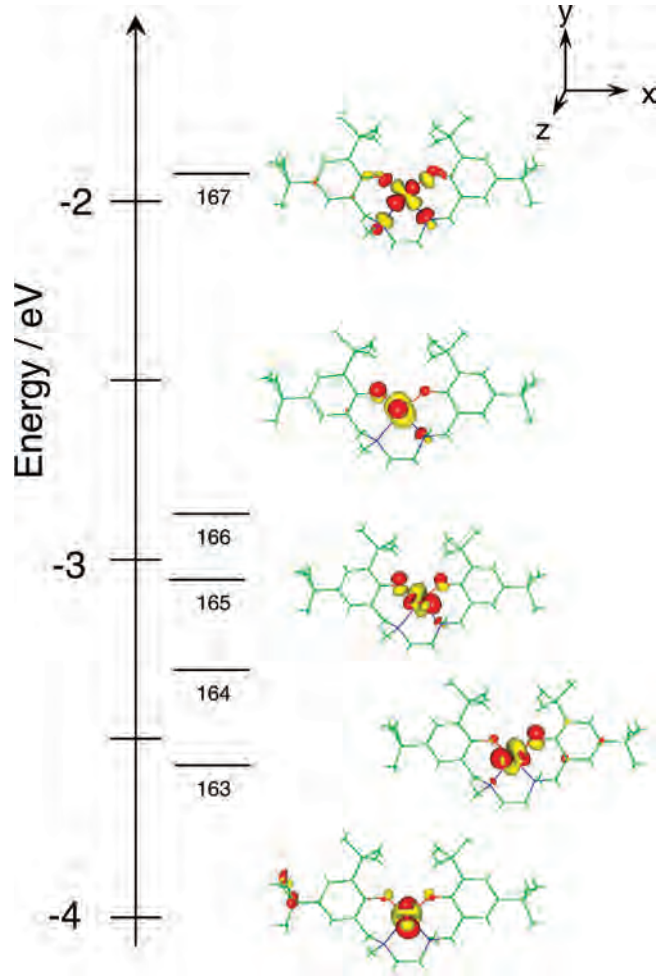

Figure 8. Spin-down metal d-based molecular orbitals for [LFeCl].

3.8. XAS Spectroscopy: Fe K-edges. The Fe K-edge X-ray absorption spectra of the complexes [LFe(η^2-NO_3)] and [LFeCl] as solutions in dichloromethane and as solids in boron nitride are depicted in Figure 9 with an expansion of the pre-edge region given in the insets. Figure S2 shows that the edges for each complex are essentially identical in solid and solution. The spectra of [LFe(μ_2-O)FeL] are included in Figure 9 for comparison.[54] The pre-edge feature of [LFe(η^2-NO_3)] occurs at 7113.7 eV and exhibits a shoulder at 7112.6 eV, while the pre-edge feature of [LFeCl] occurs at 7113.1 eV with a shoulder at 7114.3 eV. The rising edge of [LFe(η^2-NO_3)] appears at ~7123.0 eV. For [LFeCl], the rising occurs at ~7122.0 eV. This is consistent with the replacement of a light atom by a chlorine and may be attributed to a shakedown transition.[54,90]

The metal K pre-edge features of first-row transition metal complexes correspond to 1s → 3d transitions.[91] These transitions are electric quadrupole allowed but electric dipole forbidden. However, the pre-edge peaks may gain intensity through 4p mixing with the 3d orbitals in a noncentrosymmetric environment, thus giving the transition a dipole-

(90) Kau, L.-S.; Spira-Solomon, D. J.; Penner-Hahn, J. E.; Hodgson, K. O.; Solomon, E. I. *J. Am. Chem. Soc.* **1987**, *109*, 6433–6442.
(91) Shulman, R. G.; Yafet, Y.; Eisenberger, P.; Blumberg, W. E. *Proc. Natl. Acad. Sci. U.S.A.* **1976**, *73*, 1384–1388.

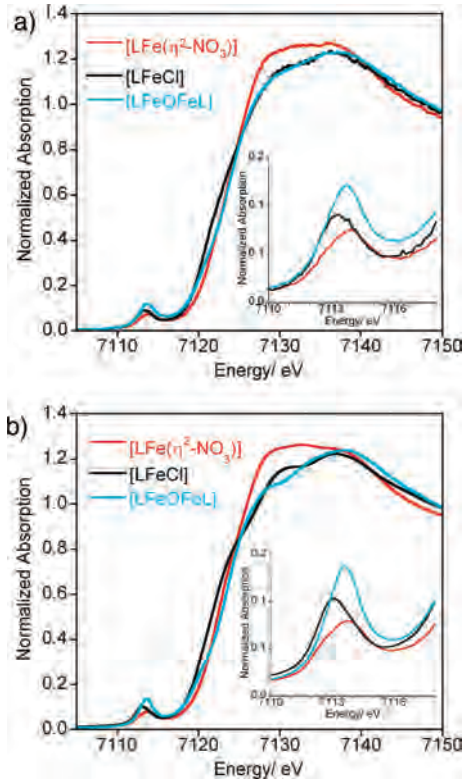

Figure 9. Comparison of the normalized Fe K-edge data for [LFe(η^2-NO_3)] and [LFeCl] (a) as solutions in dichloromethane and (b) as solids in BN. The insets show an expansion of the pre-edge region. The spectra for [LFeOFeL] are included for comparison.[54]

allowed intensity mechanism.[92,93] The pre-edge intensities of [LFeCl] and [LFe(η^2-NO_3)] are roughly three to four times more intense than that of Fe^{III} complexes with rigorously octahedral coordination environments. This indicates severe distortions from centrosymmetry for both [LFeCl] and [LFe(η^2-NO_3)]. In the case of [LFeCl], the local symmetry is C_s, and so, an intense pre-edge feature might be readily predicted. For the 6-coordinate [LFe(η^2-NO_3)], one might initially expect a weak pre-edge on the basis of the previous work of Westre et al.;[93] however the inversion symmetry is lost because of the strong asymmetry of the metal−ligand bond lengths. In both cases, the loss of inversion symmetry provides a mechanism for increased pre-edge intensity, corresponding to 15.4 and 13.7 units of intensity for [LFeCl] and [LFe(η^2-NO_3)], respectively.

The pre-edge feature of [LFeCl] is very similar to that of [(salen)FeCl] with the pre-edge of [LFeCl] being slightly broader than that of [(salen)FeCl].[93] The high intensity of the pre-edge features indicates that these transitions are primarily electric dipole in origin because of the significant 4p character in the 3d-orbitals (see section 3.7.), rather than electric quadrupole transitions. Thus, MOs 163−166 contribute to the main pre-edge feature at 7113.1 eV (with a total of ∼5% 4p character), while the higher energy shoulder at 7114.3 eV may be attributed to a transition to MO 167 (with ∼1% 4p character).

Figure 9 also shows a comparison of the square-pyramidal coordinated iron in [LFeCl] to the square-pyramidal coordinated iron in [LFe(μ_2-O)FeL]. The rising edge positions are difficult to compare because of the presence of Cl in the former, which tends to shift the rising edge to lower energy. This feature has been previously attributed to a shakedown transition.[90] Comparison of the pre-edge features however is more straightforward because the energies of these features are dominated by ligand field effects.[94] The pre-edge feature in [LFe(μ_2-O)FeL] (7113.6 eV) is ∼0.5 eV higher in energy than the pre-edge feature in [LFeCl] (7113.1 eV). For both complexes, the main component of the pre-edge feature is the transition to the d_{z^2} orbital. This increase in the energy of the d_{z^2} orbital may be attributed to the short 1.87 Å Fe−O distance in [LFe(μ_2-O)FeL], which also provides a mechanism for increased pre-edge intensity.

3.9. XAS Spectroscopy: EXAFS. [LFe(η^2-NO_3)]. Figure 10 shows the k^3-weighted EXAFS (solid line) and the fits (dashed line) for [LFe(η^2-NO_3)] as a solid (top) and as a solution in dichloromethane (bottom). It is clear that the solid and solution state differ, indicating a structural change upon solvation. Examination of the corresponding Fourier transforms (k = 2−11 $Å^{-1}$, Figure 10, right panel) indicate that the solution is much more disordered than the solid. The best fit to solid [LFe(η^2-NO_3)] (Table 6) includes 2 Fe−O interactions at 1.88 Å and 4 Fe−N/O interactions at 2.18 Å, with additional outershell contributions from light atoms at 2.97, 2.60, and 3.84 Å. The four Fe−C interactions correspond to scattering from the carbons of the benzene rings. The 2.60 and 3.84 Å contributions correspond to Fe−N and Fe−N−O interactions with the Fe-NO_3 unit. The first shell distances are in good agreement with the crystallographically determined $Fe-O^{Ph}$ bonds (1.86 Å) and the average distance of the remaining Fe−N/O bonds (2.19 Å). For the [LFe(η^2-NO_3)] solution sample, the data are best fit by inclusion of 2 Fe−O interactions at 1.88 Å, 4 Fe−N/O interactions at 2.12 Å, and additional light atom contributions at 2.99, 2.55, and 3.83 Å, with the same origin as in the solid complex. Because the $Fe-O^{Ph}$ bond lengths are unchanged in solution and the outershell contributions from the ligand L^{2-} are also essentially the same, this suggests the largest structural change is likely attributed to the coordination mode of the NO_3^-. The decrease in the 2.60 Å Fe−N (of the Fe−NO_3 unit) by ∼0.05 Å further supports this.

[LFeCl]. The k^3-weighted EXAFS (solid line) and the fits (dashed line) for [LFeCl] as a solid (top) and as a solution in CH_2Cl_2 (bottom) are shown in Figure 11. The corresponding Fourier transforms (k = 2−11 $Å^{-1}$) are shown on the right. The overall beat patterns differ, again indicating that there are differences between the solid and solution states. Table 6 summarizes the best fits to the data. For solid [LFeCl] the best fit is obtained by inclusion of two Fe−O interactions at 1.86 Å and one Fe−Cl at 2.27 Å, with additional outershell contributions from L^{2-} at 2.97 and 4.74 Å. The first-shell Fe−O and Fe−Cl distance are within error of the crystal-

(92) Randall, C. R.; Shu, L.; Chiou, Y.-M.; Hagen, K. S.; Ito, M.; Kitajima, N.; Lachicotte, R. J.; Zang, Y.; Que, L., Jr. *Inorg. Chem.* **1995**, *34*, 1036–1039.
(93) Westre, T. E.; Kennepohl, P.; Dewitt, J. G.; Hedman, B.; Hodgson, K. O.; Solomon, E. I. *J. Am. Chem. Soc.* **1997**, *119*, 6297–6314.
(94) Sarangi, R.; Aboelella, N.; Fujisawa, K.; Tolman, W. B.; Hedman, B.; Hodgeson, K. O.; Solomon, E. I. *J. Am. Chem. Soc.* **2006**, *128*, 8286–8296.

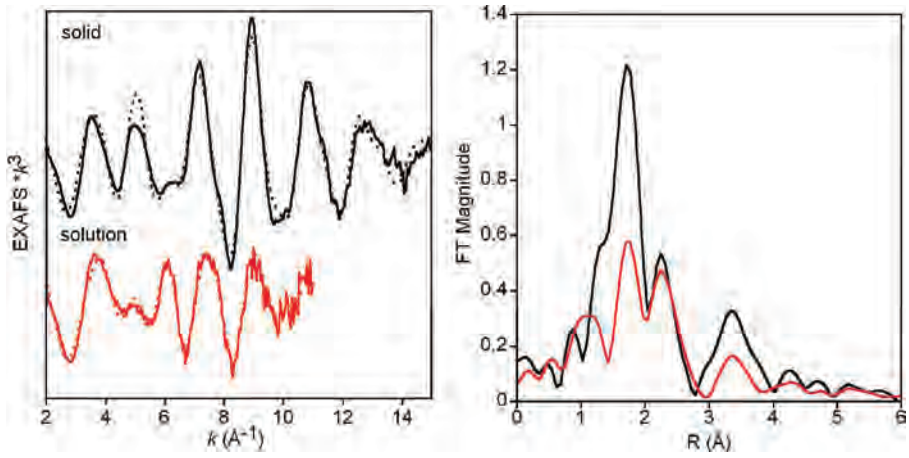

Figure 10. (left) Comparison of the EXAFS data (solid lines) and the fits to the data (dashed lines) for solid (black) and solution (red) [LFe(η^2-NO_3)] and (right) the corresponding nonphase shift corrected Fourier transforms. For comparison, a k range of 2−11 Å^{-1} has been used for both FTs.

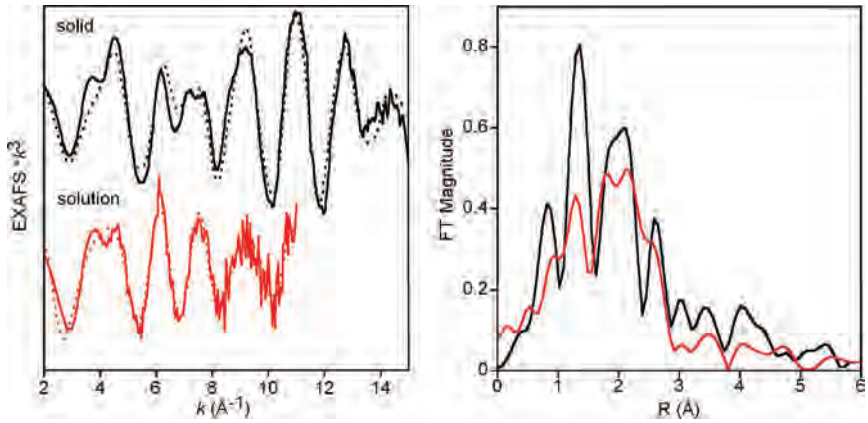

Figure 11. (left) Comparison of the EXAFS data (solid lines) and the fits to the data (dashed lines) for solid (black) and solution (red) [LFeCl] and (right) the corresponding nonphase shift corrected Fourier transforms. For comparison, a k range of 2−11 Å^{-1} has been used for both FTs.

Table 6. EXAFS Fit Results for [LFe(η^2-NO_3)] and [LFeCl] as a Solid and in Dichloromethane Solution

solid [LFe(η^2-NO_3)]			solution [LFe(η^2-NO_3)]			solid [LFeCl]			solution [LFeCl]		
	R (Å)	σ^2 (Å^2)		R (Å)	σ^2 (Å^2)		R (Å)	σ^2 (Å^2)		R (Å)	σ^2 (Å^2)
2 Fe−O	1.88	0.0028	2 Fe−O	1.88	0.0028	2 Fe−O	1.86	0.0030	2 Fe−O	1.89	0.0013
4 Fe−N/O	2.18	0.0064	4 Fe−N/O	2.12	0.0102	1 Fe−Cl	2.27	0.0029	1 Fe−Cl	2.28	0.0045
4 Fe−C	2.97	0.0082	4 Fe−C	2.99	0.0106	4 Fe−C	2.97	0.0050	4 Fe−C	2.99	0.0061
1 Fe−N	2.60	0.0059	2 Fe−N	2.55	0.0019	4 Fe−C	4.74	0.0053	4 Fe−C	4.74	0.0092
2 Fe−O	3.84	0.0045	2 Fe−O	3.83	0.0099						
ΔE_0	−1.13		ΔE_0	−0.17		ΔE_0	−3.25		ΔE_0	−2.73	
error[a]	0.147		error[a]	0.133		error[a]	0.345		error[a]	0.299	

[a] Error is given by $\Sigma(\chi_{obsd} - \chi_{calcd})^2k^6]/\Sigma(\chi_{obsd}{}^2k^6]$.

lographically determined distances (vide supra). However, no Fe−N interactions were required to fit the data. Attempts to include an 2.16 or 2.28 Fe−N interactions resulted in refined distances of 2.19−2.26 Å with Debye−Waller values of 0.02 Å^2 or larger, indicating that the component makes no significant contribution to the EXAFS data. This may be attributed to the fact that the slightly shorter and slightly longer Fe−N contributions may be out of phase resulting in a net cancellation in the total signal; however, outer-shell contributions from L^{2-} are still present at longer distances. A similar situation is observed for the [LFeCl] solution. The data require two Fe−O interactions at 1.89 Å and one Fe−Cl at 2.28 Å, with additional contributions from L^{2-}. Fe−N interactions were no longer required to fit the data.

It is of interest to note that, despite the changes in solid and solution state EXAFS data for both [LFeCl] and [LFe(η^2-NO_3)], no dramatic changes are observed in the edge data. One might expect that the decrease in the distance of the four Fe−N/O interactions in [LFe(η^2-NO_3)] from 2.18 to 2.12 Å on going from solid to solution would also impact the edge data, in particular the pre-edge region, which has been shown to be a very sensitive probe of the local geometric structure.[93]

3.10 Electrochemistry. Cyclic voltammograms (CVs) and square-wave voltammograms (SWs) of [LFe(η^2-NO_3)] and [LFeCl] have been recorded in dichloromethane solutions containing 0.20 M [N(n-Bu)$_4$]PF_6 as a supporting electrolyte (Figure 12). Small amounts of ferrocene were added after the completion of each set of experiments as an internal

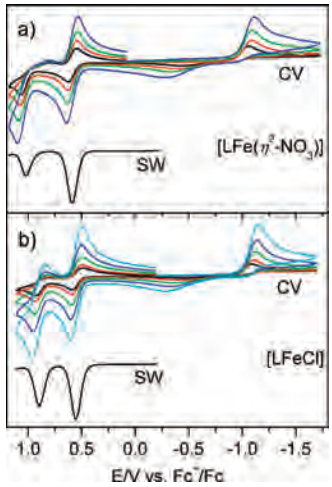

Figure 12. Cyclic voltammograms and square-wave voltammograms of (a) [LFe(η^2-NO_3] and (b) [LFeCl] in dichloromethane (0.2 M [(n-Bu)$_4$N]PF_6) at 20 °C recorded at a glassy carbon working electrode versus a Ag/$AgNO_3$ reference electrode. Scan rates for CV: 50 (black line), 100 (red), 200 (green), 400 (blue), and 800 (light blue) mV/s. Frequencies for SW: (a) 15 Hz and (b) 25 Hz.

standard, and all potentials are referenced versus the Fc^+/Fc couple.

[LFe(η^2-NO_3)]. Figure 12a displays the CVs and the SW of [LFe(η^2-NO_3)] at scan rates of 50−400 mV/s and a frequency of 15 Hz, respectively. At a velocity of 100 mV/s, [LFe(η^2-NO_3)] exhibits one irreversible reduction wave at $E^1_{p,red} = -1.09$ V, one reversible oxidation wave at $E^2_{1/2} = +0.59$ V, and one irreversible oxidation wave at $E^3_{p,ox} = +1.07$ V ($E_{p,red}$ and $E_{p,ox}$ denote the peak potentials for reduction and oxidation, respectively). The oxidative peak currents of the reversible wave at $E^2_{1/2}$ are similar to the ones of the irreversible wave at $E^3_{p,ox}$.

[LFeCl]. The CVs of [LFeCl] at scan rates of 50−800 mV/s and the SW at a frequency of 25 Hz are depicted in Figure 12b. In a manner similar to that of [LFe(η^2-NO_3)], [LFeCl] exhibits one irreversible reduction wave at $E^1_{p,red} = -1.10$ V, one reversible oxidation wave at $E^2_{1/2} = +0.55$ V, and one irreversible oxidation wave at $E^3_{p,ox} = +0.93$ V at a velocity of 100 mV/s. However, while the ratios of the currents I_{red}/I_{ox} for $E^3_{p,ox}$ at small velocities (50 mV/s) is below 1, it approaches 1 with increasing scan rates up to 800 mV/s ($E^3_{p,ox} = +0.96$ V and $E^3_{p,red} = +0.84$ V). Thus, at high velocities, the rereduction becomes kinetically competent to a chemical reaction of double-oxidized $[LFeCl]^{2+}$. Similar to [LFe(η^2-NO_3)], the peak current of the wave at $E^2_{1/2}$ is nearly as high as the peak current of the wave at $E^3_{p,ox}$.

It is interesting to note that $E^2_{1/2}$ and $E^3_{p,ox}$ of [LFeCl] are shifted cathodically by 40 and 140 mV, respectively, in comparison to the corresponding potentials of [LFe(η^2-NO_3)] (at a scan rate of 100 mV/s), that is, oxidized $[LFeCl]^+$ is stabilized in comparison to $[LFe(\eta^2\text{-}NO_3)]^+$. The irreversible reductions E^1 at negative potentials might be initiated by the Fe^{III}/Fe^{II} couple and will not be discussed further.

3.11 Spectroelectrochemistry. Chronoamperometric experiments with [LFeCl] dissolved in dichloromethane at −20 °C were performed by using an optically transparent thin-layer electrochemical cell (OTTLE cell, $d = 0.018$ cm). The thin layer of the cell enables a fast oxidation of the contained solution. UV−vis spectra were recorded in situ during electrolysis. This allowed for the progress of the oxidation to be followed and the electronic spectra of the oxidized complexes to be measured.

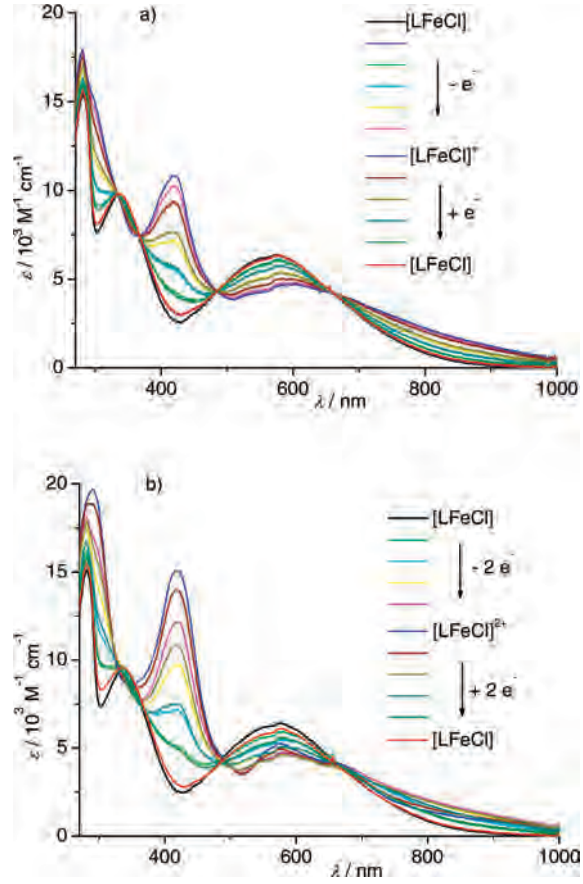

Figure 13. UV−vis spectra recorded during a chronoamperometry of [LFeCl] in dichloromethane (0.2 M [N(n-Bu)$_4$]PF_6) in an OTTLE cell at −20 °C. A glassy carbon working electrode and an Ag-wire reference electrode were used. The UV−vis spectra recorded at the beginning and at the end of the chronoamperometry are almost identical. (a) The voltage was increased from 0.2 to 0.7 V and then reduced to 0.1 V vs Fc/Fc^+. (b) The voltage was increased from 0.2 to 1.1 V and then reduced to 0.1 V vs Fc/Fc^+.

For the first one-electron oxidation of [LFeCl], the voltage was increased from 0.2 to 0.7 V vs Fc^+/Fc within 70 s and then cycled back to 0.1 V vs Fc^+/Fc. The UV−vis spectra recorded during the electrolysis are depicted in Figure 13a. During increase of the voltage, the spectra exhibit a strong increase of the absorption at 420 nm ($\varepsilon > 10\,000$ M^{-1} cm^{-1}). Moreover, the extinction coefficient at 600 nm decreases and increases at 800 nm. Upon cycling back, the absorptions at 420 and 800 nm decrease, while the extinction coefficient at 600 nm increases. At 0.2 V vs Fc^+/Fc, the spectrum of the starting complex [LFeCl] is reproduced, and the UV−vis spectra exhibit isosbestic points at 335, 367, 486, and 659 nm.

An absorption band at ∼ 400 nm is characteristic for phenoxyl radicals.[34,95,96] Thus, the strong increase in the absorption at 420 nm indicates the formation of a Fe^{III} phenoxyl radical species. The reproduction of the spectrum of the starting complex [LFeCl] at the end of the chronoamperometry and the existence of isosbestic points show that

the first one-electron oxidation of [LFeCl] to produce the Fe^{III} phenoxyl radical species $[LFeCl]^+$ is reversible on the time scale of this electrochemical experiment.

To obtain the two-electron oxidized species $[LFeCl]^{2+}$, the voltage was increased from 0.2 to 1.1 V vs Fc^+/Fc over a period of 70 s. Thereafter, cycling back was stopped at a voltage of 0.1 V vs Fc^+/Fc. The UV−vis spectra recorded during the full cycle are presented in Figure 13b. Similarly to the one-electron oxidation, the absorption at 420 nm increases constantly while the voltage is increased. It should be noted that the extinction coefficient at 420 nm for the two-electron oxidation is significantly higher ($\varepsilon > 15000\ M^{-1}\ cm^{-1}$) in comparison to the one-electron oxidation. Furthermore, the extinction coefficient at 600 nm decreases and the absorption at 800 nm increases. Upon cycling back, the absorptions at 420 and 800 nm decrease, while the extinction coefficient at 600 nm increases. When 0.1 V vs Fc^+/Fc is reached, the spectrum of the neutral starting complex [LFeCl] is almost reproduced. However, it is not as well reproduced compared to the one-electron oxidation. Although the monocation and the dication are formed one after another, the UV−vis spectra exhibit relatively well defined isosbestic points at ∼ 335, 367, 486, and 659 nm. This implies that the two oxidation processes resulting in the formation of the monocation and of the dication are of similar type.

Similarly to the formation of the one-electron oxidized species $[LFeCl]^+$, the increase of the absorption at 420 nm indicates that a phenoxyl radical species is formed. The significantly higher extinction coefficient and its constant increase indicate that $[LFeCl]^{2+}$ is a Fe^{III} diphenoxyl radical species. A spectrum nearly identical to the starting material [LFeCl] is obtained after cycling back the voltage indicating that the formation of the Fe^{III} diphenoxyl radical species $[LFeCl]^{2+}$ at −20 °C is nearly reversible on the time scale of this chronoamperometry.

4. Discussion

4.1. Structural Variability of the Ligand in Solid State. For a linear mononucleating ligand with four donor atoms, such as H_2L, three different conformations are possible.[78] In the case of the α-cis and β-cis conformations, three of the donor atoms are in a plane, while the fourth donor atom is out of plane. For a trans conformation, all donor atoms are in plane. The ligand L^{2-} in [LFeCl], in which the iron atom is five-coordinate, adopts a trans conformation, whereas in six-coordinate $[LFe(\eta^2\text{-}NO_3)]$, L^{2-} adopts a β-cis conformation. This indicates the high flexibility of the ligand with only small differences in the energies of both conformations.

4.2. Electronic Structure. The initial motivation for this study was the substitution of two weakly electron-donating pyridine rings in BPMCN by two strongly electron-donating phenolate rings in H_2L (Scheme 2). The combined spectroscopic and computational investigations performed in this study allow for the elucidation of the electron-donating capabilities of the phenolate donors and hence the covalency of the Fe^{III}−phenolate bond.

The oxygen atoms of free phenolates possess three filled p-orbitals. The p-orbital that is oriented along the C−O bond is involved in σ-bonding to the carbon atom.[79] It is the lowest in energy and thus is not expected to contribute to the bonding to coordinated metal ions.[80] One of the remaining p-orbitals lies in the plane of the aromatic ring (p_π^{ip}), while the other one lies perpendicular to the aromatic ring (p_π^{op}). Principally, these orbitals can both be involved in metal−phenolate bonding. Even in highly symmetric coordination geometries around the metal center, the bonding characteristics with respect to the metal ion (σ vs π) of p_π^{ip} and p_π^{op} (here π denotes the bonding characteristics with respect to the O−C bond) depend on the Fe−O^{Ph}−C angle and the Fe−O−C−C dihedral angle.[79] In Fe^{III} tris(catecholate) complexes, the $p_\pi \rightarrow d_{\pi^*}$ and $p_\pi \rightarrow d_{\sigma^*}$ CT transitions all involve the p_π^{op}-orbitals of the catecholate.[80] In the more asymmetric coordinate environment of the active site in 3,4-PCD, the two p_π^{ip}- and p_π^{op}-orbitals of each tyrosinate mix strongly with the Fe d-orbitals. An assignment to pure σ- and π-bonding is thus not feasible.[79]

The bonding in salen-like five-coordinate metal complexes with a square-pyramidal coordination environment is often discussed in approximate C_{4v} symmetry. This implies equal bonding contributions from the N-donors and the O-donors of the salen-like ligand. However, the bonding characteristics of phenolate versus imine/amine donors differ strongly. A more appropriate description arises from an approximate C_s symmetry as observed in [LFeCl]. This symmetry requires as a drawback a coordinate system different from that usually applied to octahedral complexes. The x- and y-axes bisect the angles formed by the donor atoms of the equatorial ligands and the iron atom (Figure 8). The "e-set" is thus composed of the d_{xy} and d_{z^2} orbitals while the "t_2-set" is composed of the d_{xz}, d_{xy}, and $d_{x^2-y^2}$ orbitals. Starting from a pure σ-square pyramidal complex (C_{4v}), the e-set splits in energy stabilizing the d_{z^2}-orbital and strongly destabilizing the d_{xy}-orbital in energy. In addition, the t_2-set splits to a minor degree resulting in slightly stabilized d_{xz} and d_{yz} orbitals. However, in salen-like and in salan-like metal complexes, as in [LFeCl], the π-donor ability of the phenolates strongly perturbs this simplified picture.

The three t_2-orbitals are strongly mixed to form two suitable π-acceptor orbitals for the two phenolate π-donors. The iron atom in [LFeCl] is situated 0.51 Å above the equatorial plane. This allows the d_{xz} and $d_{x^2-y^2}$ orbitals to mix forming two π-acceptor orbitals (MO 164 and 165, d_π^{eq1} and d_π^{eq2}, respectively, Figure 8 and Table 5). The remaining d_{yz} orbital is mainly involved in π-bonding to the axial Cl^- ligand (MO 163, d_π^{ax}). The d-orbital splitting shown in Figure 8 implies a strong deviation from a C_{4v} orbital splitting for [LFeCl] indicating the magnitude of the π-donor strength of the phenolates. This is also corroborated by 11.9% and 9.3% O^{Ph} atom contribution to d_π^{eq1} and d_π^{eq2}, respectively. An additional indication for the strong electron-donating

(95) Land, E. J.; Porter, G.; Strachan, E. *Trans. Faraday Soc. (London)* **1960**, *57*, 1885–1893.
(96) Sokolowski, A.; Müller, J.; Weyhermüller, T.; Schnepf, R.; Hildebrandt, P.; Hildenbrand, K.; Bothe, E.; Wieghardt, K. *J. Am. Chem. Soc.* **1997**, *119*, 8889–8900.

capacity of the phenolate donors yields the comparison of the overall O^{Ph} character to the overall N character of the five mainly d-based orbitals: The overall O^{Ph} character is 39.7%, while the overall N character is less than half of this (16.8%). These differences in the bonding result in an overall anisotropic covalency that is experimentally probed by several spectroscopic methods.

The quadrupole splitting ΔE_Q in Fe^{III} h. s. complexes is a good measure for the deviation from a spherical electron-density around the Fe nucleus, which is expected for a pure octahedral Fe^{III} complex ($\Delta E_Q = 0$). The presence of different types of ligands yields a perturbation from pure octahedral symmetry, and therefore small anisotropies in the electron density around the nucleus, which may be subdivided into a so-called lattice contribution because of differences in the surroundings of the iron atom and a so-called valence contribution caused by small bonding differences to the respective ligand atoms.[97] Typical values for six-coordinate Fe^{III} h.s. complexes with different types of ligands are quadrupole splittings up to 0.7 mm s^{-1}. Well known exceptions are oxo-bridged diferric complexes, which exhibit quadrupole splittings up to 2.2 mm/s.[98–100] In this respect, the quadrupole splitting of $\Delta E_Q = +1.24$ mm/s for [LFeCl] is a strong indication for a highly anisotropic electron density around the Fe nucleus in a nonoxo-bridged Fe^{III} complex and can be easily assigned to the strong anisotropy in the covalency resulting from the strong σ- and π-donating phenolate donors in cis-position. Moreover, while the quadrupole splitting of oxo-bridged diferric complexes have a negative sign, the sign of the quadrupole splitting in [LFeCl] is positive. This demonstrates the difference in the anisotropy of the electron density. The short Fe−O-bond in oxo-bridged Fe^{III} complexes results in an axially elongated electron density (prolate), whereas the strong phenolate donors in one plane result in an axially compressed electron density (oblate).

Another experimental indication for the strong covalency is the reduced isotropic hyperfine coupling tensor obtained from Mössbauer spectroscopy with applied magnetic fields.

An additional independent experimental probe for the anisotropy of the covalency is the zero-field splitting. The zero-field splitting in an octahedral Fe^{III} h.s. complex is expected to be zero. For zero-field splitting to occur, a deviation from pure cubic symmetry and spin−orbit coupling of excited states into the ground-state are required. A deviation from octahedral symmetry usually arises from different donor atoms, which lead to small values for D ($|D| < 0.5$ cm^{-1}). The experimentally derived values for [LFeCl] ($D = +1.15$ cm^{-1}) and [LFe(η^2-NO_3)] ($|D| = 1.2$ cm^{-1}) by use of the complementary methods magnetometry, EPR, and Mössbauer spectroscopy (with and without applied field) are quite large for mononuclear Fe^{III} complexes. The origin of this relatively strong zero-field splitting may again be attributed to the strong anisotropic covalency.[101]

The value for $E/D = 1/3$ in [LFe(η^2-NO_3)] is consistent with the cis-conformation of the ligand, providing a full rhombicity. On the other hand, the E/D value for [LFeCl] of 0.175 indicates (a) the deviation of the electronic structure from C_{4v} to C_s and (b) the overall strong electron-donating capability of L^{2-} in one plane, which precludes meeting the rhombic limit.

Both complexes [LFe(η^2-NO_3)] and [LFeCl] exhibit two intense charge-transfer (CT) bands assigned to $p_\pi \rightarrow d_{\sigma^*}$ and $p_\pi \rightarrow d_{\pi^*}$ transitions. The $p_\pi \rightarrow d_{\pi^*}$ transitions in the both complexes [LFe(η^2-NO_3)] and [LFeCl] are intense and at low energy, indicating a substantial π-bonding and thus a significant overlap of the p_π-orbitals with the metal orbitals.

The energies of the $p_\pi \rightarrow d_{\pi^*}$ CT transitions are highly dependent on the solvent and exhibit significant differences for [LFe(η^2-NO_3)] and [LFeCl]. This indicates that the $p_\pi \rightarrow d_{\pi^*}$ CT transitions are dependent on the coordination sphere of the iron atom. Variations in the coordination sphere will lead to different Fe−O−C angles and Fe−O−C−C dihedral angles which greatly influence the phenolate bonding interactions. It has been shown that the overall bonding interactions increase with decreasing Fe−O−C angle.[79] X-ray crystallography provides Fe−O−C angles for [LFe(η^2-NO_3)] incorporating the β-cis coordinating ligand (123.2° and 133.0°) that are smaller than for [LFeCl] incorporating the trans coordinating ligand (136.1° and 129.4°). Thus, the β-cis coordinating ligand may donate more charge to the iron atom and the Fe−O^{Ph} bonds in [LFe(η^2-NO_3)] can be expected to be stronger than in [LFeCl]. This is corroborated by the UV−vis spectra, where the $p_\pi \rightarrow d_{\pi^*}$ CT transitions are shifted to lower energy for [LFe(η^2-NO_3)] in comparison to [LFeCl].

4.3. Solvent Dependence of the Molecular Structures in Solutions. While a detailed understanding of the molecular structure in the solid state is needed to correlate structural, electronic, and spectroscopic properties, it is necessary to have experimental insight into the molecular structure in solution to understand the solution reactivity at a molecular level. Despite the potential of the ligand L^{2-} to accumulate oxidation equivalents in iron complexes, it is necessary that these complexes offer free coordination sites for potential substrates. The closely related family of salen-type ligands are well-known for adopting a trans-conformation in metal complexes, when the additional coordination sites are occupied by monodentate ligands.[102,103] Only the use of bidentate ligands forces salen ligands into a cis-conformation.[104] Nevertheless, the cis-conformation is discussed as the active salen−metal−oxo species, for example, during the

(97) Gütlich; P.; Ensling, J. In.; *Mössbauer Spectroscopy, Inorganic Electronic Structure and Spectroscopy*; Solomon, E. I., Lever, A. B. B., Eds.; John Wiley and Sons: New York; 1999; Vol. *1*:Methodology.
(98) Debrunner, P. G. *Hyperfine Interact.* **1990**, *53*, 21–36.
(99) Rodriguez, J. H.; Xia, Y.-M.; Debrunner, P. G.; Chaudhuri, P.; Wieghardt, K. *J. Am. Chem. Soc.* **1996**, *118*, 7542–7550.
(100) Que, L., Jr.; True, A. E. *Prog. Inorg. Chem.* **1990**, *38*, 97–200.
(101) Neese, F.; Solomon, E. I. In *Magnetism: Molecules to Materials*, Miller, J. S., Drillon, M., Eds.; Wiley-VCH: Weinheim, Germany, 2003; Vol. *IV*, pp 345−466.
(102) Holm, R. H.; Everett, G. W.; Chakravorty, A. *Prog. Inorg. Chem.* **1966**, *7*, 83–214.
(103) Pyrz, J. W.; Roe, L.; Stern, L. J.; Que, L., Jr. *J. Am. Chem. Soc.* **1985**, *107*, 614–620.
(104) Lauffer, R. B.; Heistand, R. H., II.; Que, L., Jr. *Inorg. Chem.* **1983**, *22*, 50–55.

epoxidation of olefins.[105,106] The need to use a bidentate ligand to obtain a *cis*-conformation of salen-type ligands indicates that metal complexes with salen-type ligands of *trans*-conformation are energetically more favored.

The potential applications of iron complexes with the ligand L^{2-} in oxidative transformations require some flexibility of free coordination sites, cis or trans to each other. Spectroscopic studies using FT-IR, UV−vis, EPR, and XAS of [LFe(η^2-NO_3)] and [LFeCl] allowed us to obtain insight into the molecular structures of the complexes in solution and their flexibilities. The differences in the $p_\pi \rightarrow d_{\pi^*}$ transition of [LFe(η^2-NO_3)] and [LFeCl] in the absorption spectra measured in the nonpolar solvent *n*-pentane are an indication that the variations observed in the solid state structures remain in nonpolar aprotic solvents. Thus, in nonpolar solvents, the ligand L^{2-} adopts a β-cis conformation in [LFe(η^2-NO_3)] and a trans conformation in [LFeCl]. The variations in the absorption maxima of the $p_\pi \rightarrow d_{\pi^*}$ transitions are the result of the differences in the π-bonding (see section 4.2.).[79]

This interpretation is corroborated by EPR spectroscopy. Going from *n*-pentane to the slightly more polar but still aprotic and noncoordinating solvents dichloromethane and ethyl acetate results in different spectra with varying rhombicities *E*/*D*. The spectra of [LFe(η^2-NO_3)] exhibit rhombicities of $E/D = 1/3$, consistent with the β-cis conformation of the ligand. On the other hand, the spectra of [LFeCl] indicate the existence of a main component of ~85% with $E/D \approx 0.15$. This decrease in rhombicity is indicative of a species with a ligand in trans conformation. It is interesting to note that in these slightly more polar solvents already a second species of around 15% with a rhombicity $E/D = 1/3$ appears. Thus, [LFeCl] undergoes a structural rearrangement to a β-cis conformation in this solvent, which indicates that the energies of complexes with L^{2-} in a trans conformation and in a β-cis conformation are quite similar. These results agree well with the UV−vis spectra measured in dichloromethane and acetonitrile. The deviation of the $p_\pi \rightarrow d_{\pi^*}$ transitions in the UV−vis spectra when compared to the spectra measured in *n*-pentane (which can be taken as a standard for the two extreme coordination modes) are a good indicator for the extent of the transformation.

On the other hand, the absorption spectra of both complexes measured in methanol are almost identical, proving that the molecular structures and the conformations of the ligands are very similar. This is corroborated by the EPR spectra, which are also identical when measured on [LFe(η^2-NO_3)] and [LFeCl] dissolved in methanol. These spectroscopies (i.e., the energy of the absorption bands and the *E*/*D* value determined by the EPR spectra) clearly demonstrate that not only [LFe(η^2-NO_3)] but also [LFeCl] possess a β-cis coordinated ligand in polar protic solvents.

The observed flexibility of the ligand as evidenced by variations of the Fe−N bond lengths, the Fe−O−C bonding angles, the Fe−O−C−C dihedral angles, and the solvent-dependence of the $p_\pi \rightarrow d_{\pi^*}$ LMCT transitions indicate a flat potential energy surface for the ligand L^{2-}. This may be related to the multitude of possible bonding pathways for four O^{Ph} p_π-orbitals with the Fe d-orbitals. Diminished overlap of one bonding pathway by slightly changing one dihedral angle increases a different bonding pathway. This is related to the phenomenon of the low angle-dependence for the exchange coupling constant *J* in oxo-bridged diferric complexes. Decreasing one of the 25 possible exchange pathways by varying the Fe−O−Fe angle increases another exchange pathway and vice versa.[107–109]

A different aspect concerns the identity of the ligands at the remaining coordination sites. The IR spectrum of [LFe(η^2-NO_3)] measured in dichloromethane solution shows that there is some free NO_3^-. This is corroborated by the solution EXAFS data, which suggests that more than one species is present and that some structural variations occur. However, it is difficult to extract from this data whether the remaining coordinated nitrate ions are bound in a monodentate or bidentate fashion in dichloromethane solution. The highly resolved hyperfine-split signal at $g = 9.44$ in the EPR spectrum in butyronitrile solution and the order of magnitude of the hyperfine interaction is indicative that a water molecule is coordinated to the iron atom in addition to the ligand L^{2-} adopting a cis coordination mode. However, we do not have definite proof for this. The only definite handle for the remaining coordination sites in [LFeCl] arises from EXAFS, which clearly needs a Fe−Cl vector for the analysis of the data. Thus in dichloromethane solution, most of the iron ions are still coordinated to Cl^-.

4.4. Generation of One-Electron and Two-Electron Oxidized Species. The electrochemical studies show that Fe^{III} in [LFe(η^2-NO_3)] and [LFeCl] can be irreversibly reduced to Fe^{II}. On the anodic side, two one-electron oxidations can be carried out on both complexes. The first oxidation is reversible for both complexes. For [LFe(η^2-NO_3)], the second oxidation is more complicated, as it is irreversible on the time scale of the CV experiment even at fast scan rates. On the other hand, the two-electron oxidized species $[LFeCl]^{2+}$ exhibits a greater stability, so that the second oxidation of [LFeCl] becomes close to reversible for high scan rates. This indicates the occurrence of a kinetically competent follow-up reaction of the double-oxidized species.

The first oxidation of [LFe(η^2-NO_3)] and [LFeCl] takes place at a potential of +0.59 V and +0.55 V vs Fc^+/Fc, respectively, that is, [LFeCl] is easier to oxidize. It is interesting to discuss the origin of this small but significant shift in the potential. In [LFeCl], which incorporates the trans coordinated ligand, the phenolate p_π donor orbitals donate to d_{π^*} orbitals with strong spatial overlap. In [LFe(η^2-NO_3)], the d_{π^*} acceptor orbitals are spatially more separated allowing more efficient charge donation from phenolate donors. This more efficient charge donation in [LFe(η^2-NO_3)] is in

(105) McGarrigle, E. M.; Gilheany, D. G. *Chem. Rev.* **2005**, *105*, 1563–1602.
(106) Hamada, T.; Fukuda, T.; Imanishi, H.; Katsuki, T. *Tetrahedron* **1996**, *52*, 515–530.
(107) Norman, R. E.; Holz, R. C.; Menage, S.; Que, L., Jr.; Zhang, J. H.; O'Connor, C. J. *Inorg. Chem.* **1990**, *29*, 4629–4637.
(108) Gorun, S. M.; Lippard, S. J. *Inorg. Chem.* **1991**, *30*, 1625–1630.
(109) Weihe, H.; Güdel, H. U. *J. Am. Chem. Soc.* **1997**, *119*, 6539–6543.

agreement with the lower energy of the $p_\pi \rightarrow d_{\pi^*}$ transition. This would normally be interpreted as the electron density at the Fe^{III} ion in [LFe(η^2-NO_3)] being higher in comparison to the electron density at the Fe^{III} ion in [LFeCl]. Thus, the Fe^{III} ion in [LFe(η^2-NO_3)] should be easier to oxidize. However, the opposite is observed experimentally. This might be seen as an indication that the Fe^{III} is not oxidized, but rather a phenolate oxygen atom is oxidized. This is easier for [LFeCl] as charge donation to the Fe^{III} is less and thus the electron density at the phenolates is larger.

It is interesting to compare the oxidation of [LFeCl] to that of an analogous salen Fe^{III} complex, namely [(salen*)FeCl] (H_2salen* is a salen derivative with bulky mesityl-substituents, Scheme 1).[42,110] [(salen*)FeCl] exhibits two poorly resolved one-electron oxidation waves at 0.85 and 0.96 V vs Fc^+/Fc, that is, [LFeCl] is easier to oxidize by 0.30 V. This can be explained by the substitution of the *tert*-amines in [LFeCl] by imines in [(salen*)FeCl]. The *tert*-amines are better σ-donors and possess no π-acceptor capabilities. Therefore, they increase the electron density at the metal site more than imines. This shift is also in accordance with the shift observed for the oxidation of [(salan′)Cu] in comparison to [(salen′)Cu] ([(salan)Cu] is easier to oxidize, see Introduction).[39,40]

The formation of a well-resolved isolated absorption at 420 nm in the UV−vis spectrum of $[LFeCl]^+$ and the strong increase of this band by going to $[LFeCl]^{2+}$ are major indications that the one- and two-electron oxidations are localized on the ligand and not on the metal. Thus, the preferred ground-state description for $[LFeCl]^+$ is as an Fe^{III} phenoxyl radical species and for $[LFeCl]^{2+}$ as an Fe^{III} bisphenoxyl species. This behavior is closely related to the archetypal Fe^{III} phenoxyl radical complex incorporating a tris-phenolate derivative of 1,4,7-triazacyclononan described by Wieghardt et al.[34] This tris-phenolate Fe^{III} complex can be oxidized to the mono- and dication with the occurrence of a strong, well isolated band at 400 nm. This band nearly doubles in intensity by going from the monocation to the dication. It is interesting to compare these results to other proposed phenoxyl radical metal complexes. The spectrum of the mono-oxidized complex $[(salan')Cu]^+$ exhibits an increase in intensity with a maximum at ~410 nm. However, this band is not well resolved. In contrast, the doubly oxidized species $[(salan')Cu]^{2+}$ exhibits a strong isolated band at ~410 nm, which is nearly doubled in intensity.[39] Interestingly, the spectrum of the analogous salen derivative $[(salen')Cu]^+$ shows a band at ~390 nm, which is also present in the nonoxidized species. Thus, it is difficult to assign a real phenoxyl radical transition in $[(salen')Cu]^+$. For $[(salen^*)FeCl]^+$, the authors propose a band at ~350 nm to be indicative for a phenoxyl radical.[42] This comparison indicates that the electronic structure of phenoxyl radicals incorporating saturated salan-type ligands are different in comparison to their respective unsaturated salen-type ligands.

5. Conclusion

The strongly electron-donating ligand L^{2-} is composed of two *tert*-amines and two phenolate donor groups. The electronic structure of the mononuclear Fe^{III} complexes [LFe(η^2-NO_3)] and [LFeCl] is governed by the strong σ- and π-donor interactions of the phenolate donors, which result in a strong anisotropic covalency and, hence, a relatively strong distortion from an isotropic $^6A_{1g}$ Fe^{III} high-spin ion in octahedral symmetry. This is experimentally evidenced by the sizable zero-field splitting parameter D and the strong quadrupole splitting ΔE_Q. The UV−vis bands and the E/D ratios provide good indications for the molecular structure of the complexes in solution. The solution studies establish a high flexibility of the ligand L^{2-}. The cis and trans conformations are close in energy and the predominant conformation can be influenced by the polarity of the solvent. In polar and protic solvents the cis conformation with two free coordination sites open for possible substrates prevails.

The cis arrangement of the two free coordination sites occurs along with a cis arrangement of the two phenolate donors. This is a feature also present in the active site of native 3,4-PCD with a His_2Tyr_2 donor set provided by the protein and completed by an OH^- ligand. The occurrence of the phenolate-to-Fe^{III} LMCT transition in 3,4-PCD at 460 nm[111] as compared to 610 nm in [LFe(η^2-NO_3)] demonstrates the strong σ- and π-donor capabilities of the OH^- ligand. The latter increases the electron density at the Fe^{III} ions which leads to a shift of the LMCT to higher energy. The OH^- ligand is thus comparable to a second $[O-FeL]^-$ metallo-ligand fragment as this metallo-ligand also shifts the phenolate-to-Fe^{III} charge transfer transition in [LFe(μ_2-O)FeL] to higher energy (435 nm).[53] The remaining difference (435−460 nm) may be attributed to the square pyramidal coordination environment of [LFe(μ_2-O)FeL] in comparison to the trigonal bipyramidal coordination environment in the native 3,4-PCD. Iron complexes with ligands related to L^{2-} have already been successfully employed as functional models with intradiol-catechol dioxygenase activity.[112–118]

The mononuclear Fe complexes of L^{2-} exhibit relatively low redox potentials for oxidation. Spectroelectrochemical methods showed an increase in the absorption of the mono- and double-oxidized forms of [LFeCl] at 420 nm, which establishes that the oxidation is mainly ligand-centered to a monophenoxyl radical Fe^{III} complex and a bisphenoxyl radical Fe^{III} complex.

(110) Fujii, H.; Funahashi, Y. *Angew. Chem., Int. Ed.* **2002**, *41*, 3638–3641.
(111) Que, L., Jr.; Epstein, R. M. *Biochemistry* **1981**, *20*, 2545–2549.
(112) Spartalian, K.; Carrano, C. J. *Inorg. Chem.* **1989**, *28*, 19–24.
(113) Mialane, P.; Anxolabehere-Mallart, E.; Blondin, G.; Nivorojkine, A.; Guilhem, J.; Tchertanova, L.; Cesario, M.; Ravi, N.; Bominaar, E.; Girerd, J. J.; Munck, E. *Inorg. Chim. Acta* **1997**, *263*, 367–378.
(114) Heistand, R. H., II; Roe, A. L.; Que, L., Jr. *Inorg. Chem.* **1982**, *21*, 676–681.
(115) Viswanathan, R.; Palaniandavar, M.; Balasubramanian, T.; Muthiah, T. P. *Inorg. Chem.* **1998**, *37*, 2943–2951.
(116) Heistand, R. H., II; Lauffer, R. B.; Fikrig, E.; Que, L., Jr. *J. Am. Chem. Soc.* **1982**, *104*, 2789–2796.
(117) Kurahashi, T.; Oda, K.; Sugimoto, M.; Ogura, T.; Fujii, H. *Inorg. Chem.* **2006**, *45*, 7709–7721.
(118) Mayilmurugan, R.; Suresh, E.; Palaniandavar, M. *Inorg. Chem.* **2007**, *46*, 6038–6049.

The main conclusion of the study is that the ligand L^{2-} provides a flexible coordination environment with two open coordination sites in addition to the storage of two oxidation equivalents close to free coordination sites. The use of these mononuclear complexes for oxidative transformations and the synthesis of high valent LFe═O species by using external oxygenation reagents such as PhIO are the focus of continuing studies by our research group.

Acknowledgment. This work was supported by the Fonds der Chemischen Industrie and the DFG. SSRL operations are funded by the Department of Energy, Office of Basic Energy Sciences. The Structural Molecular Biology program is supported by the National Institutes of Health, National Center for Research Resources, Biomedical Technology Program, and by the Department of Energy, Office of Biological and Environmental Research. This publication was made possible by Grant Number 5 P41 RR001209 from the National Center for Research Resources (NCRR), a component of the National Institutes of Health (NIH).

Supporting Information Available: Fe K-edge data for [LFe(η^2-NO_3)] and for [LFeCl] and electronic absorption spectra of [LFe(η^2-NO_3)] and of [LFeCl]. This material is available free of charge via the Internet at http://pubs.acs.org.

IC800335T